

This article has been accepted for publication in *Tectonics*.

Copyright 2021 American Geophysical Union.

Further reproduction or electronic distribution is not permitted.

1 **Inheritance of penetrative basement anisotropies by extension-oblique**
2 **faults: Insights from analogue experiments**

3

4 **Anindita Samsu¹, Alexander R Cruden¹, Nicolas E Molnar^{1,2}, Roberto F Weinberg¹**

5 ¹School of Earth, Atmosphere and Environment, Monash University, Clayton, Australia

6 ²Tectonics and Geodynamics, RWTH Aachen University, Aachen, Germany

7

8 Corresponding author: Anindita Samsu (anindita.samsu@monash.edu)

9

10 **Key Points**

- 11 • Analogue models of rifting demonstrate how extension-oblique faults in cover rocks
12 are inherited from penetrative basement anisotropies.
- 13 • The width and spacing of basement anisotropies impact the distribution, orientation,
14 and kinematics of faults in the cover.
- 15 • We invoke strain re-orientation as the mechanism for inheritance as opposed to direct
16 reactivation of basement weaknesses.

17 Abstract

18 During rifting, pre-existing penetrative basement fabrics can affect new faults in cover rocks
19 by a mechanism that does not appear to involve reactivation. This subtle form of inheritance
20 can significantly impact fault network architecture in rift basins above laterally variable
21 basement domains with geomechanical anisotropies. Here we use multi-layer, brittle-ductile,
22 crustal-scale analogue experiments to study the influence of penetrative basement
23 anisotropies on fault patterns in the overlying cover during a single phase of orthogonal
24 rifting. The experiments were designed to test whether basement anisotropies, oriented 45° to
25 the extension direction, can lead to the formation of rift faults that are oblique to both the
26 imposed extension direction and basement anisotropies. Our experiments show that a
27 penetrative, vertically layered, mm-wide basement anisotropy creates extension-oblique
28 faults in the overlying cover. We interpret this to arise when local strike-slip kinematics along
29 the interfaces of mechanically contrasting materials in the basement combine with the
30 regional imposed orthogonal extension, creating a transtensional regime. The width and
31 spacing of alternating “strong” and “weak” basement zones interact with rift kinematics,
32 impacting the orientation, kinematics and spacing of new faults in the cover. New insights on
33 the influence of penetrative, pre-existing basement fabrics on localized re-orientation of 3D
34 strain in the cover have implications for understanding complex fault systems in rift basins
35 and transfer zones.

36

37 1. Introduction

38 Pre-existing crustal weaknesses commonly influence the location, geometry, orientation, and
39 segmentation of new rifts (e.g., Brune et al., 2017; Corti et al., 2007; Daly et al., 1989; Heron
40 et al., 2019; Tommasi & Vauchez, 2001; Wilson, 1966; Zwaan & Schreurs, 2020). Many
41 natural rift systems have been impacted by the reactivation of older shear zones, including the
42 NE Brazilian margin (Kirkpatrick et al., 2013), offshore southern Norway (Phillips et al.,
43 2016), the East African Rift System (Daly et al., 1989; Heilman et al., 2019), and the
44 Australian Southern Margin (Gibson et al., 2013; Miller et al., 2002). At the scale of
45 individual rift basins, reactivation of basement structures – including discrete faults
46 (Bellahsen & Daniel, 2005; Bonini et al., 2015; Deng et al., 2017, 2018) and mechanically
47 weak layers that make up a pervasive fabric (Chattopadhyay & Chakra, 2013; Ghosh et al.,

48 2020) – during rifting can also influence the orientation, length, and kinematics of faults in
49 the overlying sedimentary cover.

50 Reactivation of weak surfaces (e.g., foliation planes) in metamorphic basement rocks
51 facilitates the nucleation of new faults along such pre-existing surfaces (Byerlee, 1978;
52 Sibson, 1985). Hence, basement reactivation gives rise to extension-oblique, rift-related faults
53 that nucleate on basement weaknesses and inherit the strike and dip direction of the basement
54 fabric (Collanega et al., 2019; Phillips et al., 2016; Rotevatn et al., 2018). As a consequence,
55 the similarity in orientation between pre-existing basement structures and new rift faults has
56 often been interpreted as evidence of basement-influenced rifting, involving reactivation of
57 the aforementioned basement structures (Beacom et al., 2001; Bird et al., 2014; Heilman et
58 al., 2019; Holdsworth et al., 1997; Kirkpatrick et al., 2013; Kolawole et al., 2018; Morley et
59 al., 2004; Peace et al., 2018). Several field studies, however, suggest that basement
60 anisotropies can influence rifting without being directly reactivated (Morley, 2010; Samsu et
61 al., 2019, 2020; Wilson et al., 2010), but the interaction between the basement anisotropies
62 and new rift faults is poorly understood.

63 In northern Scotland and southeast Australia, Wilson et al. (2010) and Samsu et al. (2019)
64 documented brittle, rift-related structures which are neither parallel to pre-existing basement
65 fabrics nor perpendicular to the inferred direction of regional extension. Variations in the
66 main orientations of rift-related faults were found across areas that overlie basement domains
67 with different metamorphic fabrics. These observations suggest that penetrative basement
68 fabrics can exert some control on the formation of new rift faults via a mechanism that does
69 not involve reactivation, but rather re-orientation of the principal stress and strain directions.
70 Analogue experiments of basement-influenced rifting by Corti et al. (2013) and Philippon et
71 al. (2015) show that stress re-orientation above a pre-existing weak zone is responsible for
72 extension-oblique faults with dip-slip kinematics at rift margins. These experiments
73 demonstrate the role of a single, underlying weak zone in forming extension-oblique, basin-
74 bounding faults, but not the influence of penetrative basement fabrics beneath sedimentary
75 basins.

76 The aim of our study is to investigate how penetrative basement anisotropies, with varying
77 widths and spacing of alternating weak and strong zones, may influence cover fault
78 orientations within rift basins. Here we use crustal-scale analogue models to demonstrate that
79 pre-existing anisotropies in the basement can form extension-oblique faults in the overlying

80 sedimentary cover by altering the 3D strain field, which signals a local perturbation of the
81 stress field. This means that oblique rift kinematic boundary conditions (Agostini et al., 2009;
82 Corti, 2008; McClay & White, 1995; Morley et al., 2004; Peace et al., 2018; Withjack &
83 Jamison, 1986) are not necessarily required to create a transtensional regime within rift
84 basins. We also show that the orientation and kinematics of rift faults is controlled by the
85 mechanical properties (e.g., strength) and geometry (i.e., the spacing and width of “weak
86 zones” that create the anisotropy) of the basement anisotropy.

87

88 **2. Experimental method**

89 Analogue modelling is a powerful tool for simulating crustal deformation in a controlled
90 environment and testing hypotheses on its tectonic driving mechanisms, using simplified
91 models that are scaled to a practical size (Ranalli, 2001). Our experiments are designed to
92 approximate a foliated basement buried under a sedimentary basin. They were inspired by the
93 western onshore Gippsland Basin, southeast Australia, which formed in the Early Cretaceous
94 during inferred N-S to NNW-SSE regional extension (Ball et al., 2013; Miller et al., 2002;
95 Williams et al., 2011). The western onshore Gippsland Basin overlies two levels of
96 anisotropic basement (Samsu et al., 2020): i) Paleozoic metasedimentary rocks of the
97 Melbourne Zone, with a NNE-SSW trending fabric, which is underlain by ii) an inferred,
98 anomalously strong Neoproterozoic–Cambrian crustal block known as the “Selwyn Block”
99 with a NE-SW structural grain (Cayley et al., 2002; Moore et al., 2016) (Fig. 1). We chose
100 this natural case as a starting point for our experiments because of the availability of multi-
101 scale structural data on the cover and of both of the basement units (Cayley et al., 2002;
102 Moore et al., 2016; Samsu et al., 2019, 2020; Vollgger & Cruden, 2016). We were further
103 motivated to better understand presently unclear relationships between Early Cretaceous rift
104 kinematics, syn-rift fault orientations, and the influence of pre-existing basement weaknesses
105 in the area (Finlayson et al., 1996; Hill et al., 1994, 1995; Samsu et al., 2019).

106 The simplified experiments represent an area that straddles the postulated eastern boundary of
107 the Selwyn Block, which trends NE-SW beneath the Gippsland Basin (Fig. 1). In the
108 sedimentary cover, faults west of this lateral basement boundary trend NE-SW to ENE-
109 WSW, while faults east of the boundary have a general E-W trend (Fig. 1b). Based on these
110 observations, we designed experiments to simulate how an anisotropic basement, such as the
111 folded and faulted turbidites of the Melbourne Zone or the “strong” Selwyn Block basement,

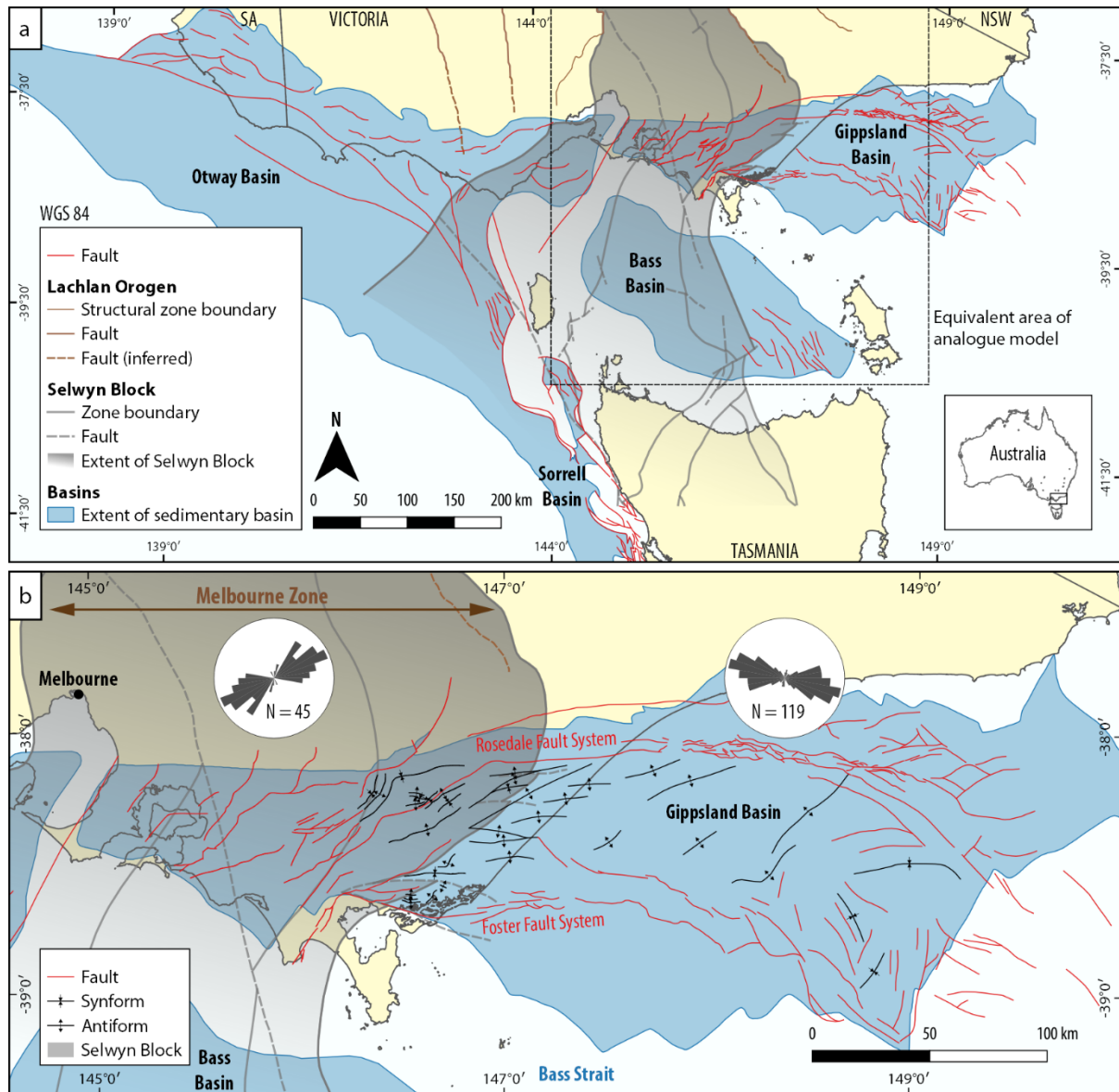
112 may impact fault patterns in the overlying cover. The models were not designed to explicitly
113 replicate the structural patterns in the Gippsland Basin but rather to provide insight on the
114 influence of basement anisotropies on syn-rift faulting.

115 2.1. Boundary and initial conditions

116 All experiments comprised a crustal-scale, brittle-ductile model lithosphere floating
117 isostatically on a fluid model asthenosphere in an acrylic tank (Fig. 2). The tank is 65 cm
118 long, 65 cm wide, and 20 cm deep. The simplified model lithosphere had an initial length and
119 width of 44 cm and 40 cm, respectively, and a thickness of 7 cm (Fig. 3). It consisted of a
120 brittle upper crust, a ductile lower crust, and a ductile lithospheric mantle. We refer to the
121 model upper crust and lower crust as “cover” and “basement”, respectively, in the remainder
122 of the paper, as we describe the relationship between anisotropic basement rocks and faulting
123 in the previously undeformed, overlying cover. The model thicknesses scale to natural layer
124 thicknesses estimated from forward modelling of geophysical potential field data (Moore et
125 al., 2016) and seismological models (Gray et al., 1998; Kennett et al., 2013) (Fig. 3 and Table
126 1). Since we did not intend to force a rift (cf. Brune et al., 2017; Zwaan et al., 2016; Zwaan &
127 Schreurs, 2017), we did not place a linear “weak zone” seed in the middle of the model.

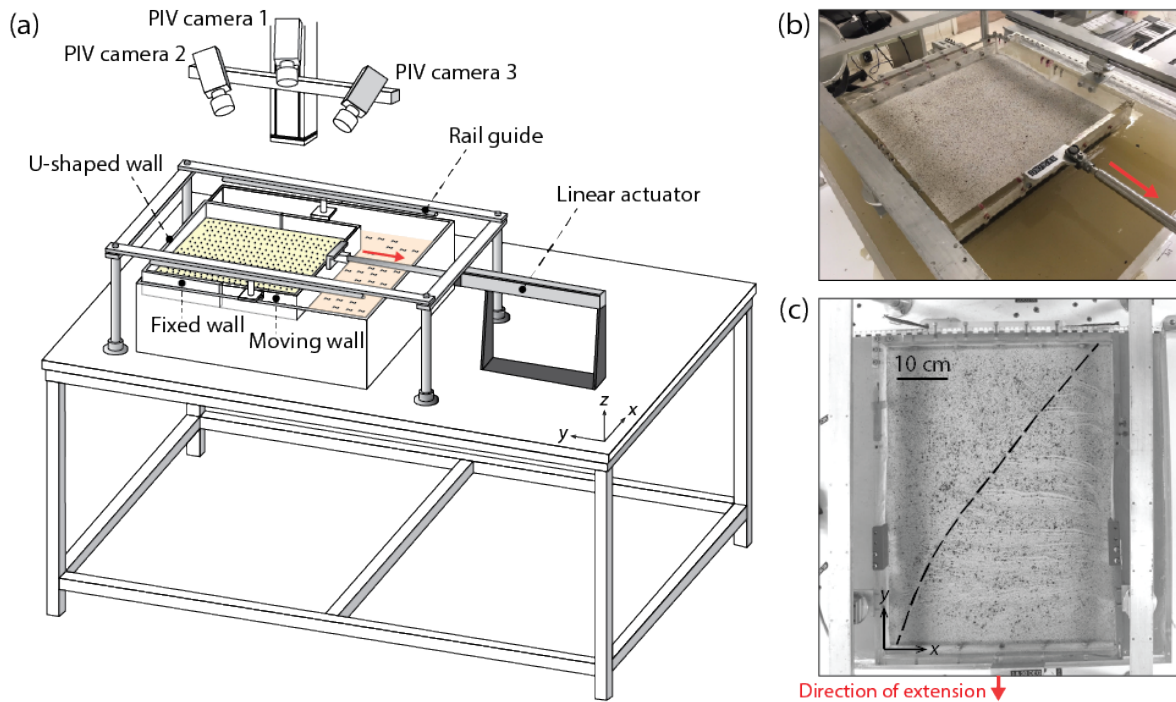
128

129



130

131 **Figure 1** (a) Map of the eastern basins of the Australian Southern Margin rift system,
 132 including the Otway, Sorrell, Gippsland, and Bass basins (modified from Samsu et al., 2019).
 133 The eastern part of the Otway Basin and the western part of the Gippsland Basin is underlain
 134 by the Paleozoic Melbourne Zone (Lachlan Orogen) basement and the Neoproterozoic–
 135 Cambrian Selwyn Block basement (Cayley et al., 2002; McLean et al., 2010). (b) Major
 136 structures of the Gippsland Basin: The rose diagrams show that faults above the Selwyn
 137 Block/Melbourne Zone trend predominantly NE-SW and ENE-WSW, while faults east of this
 138 zone trend E-W to NW-SE (modified after Constantine, 2001 and Power et al., 2001).



139

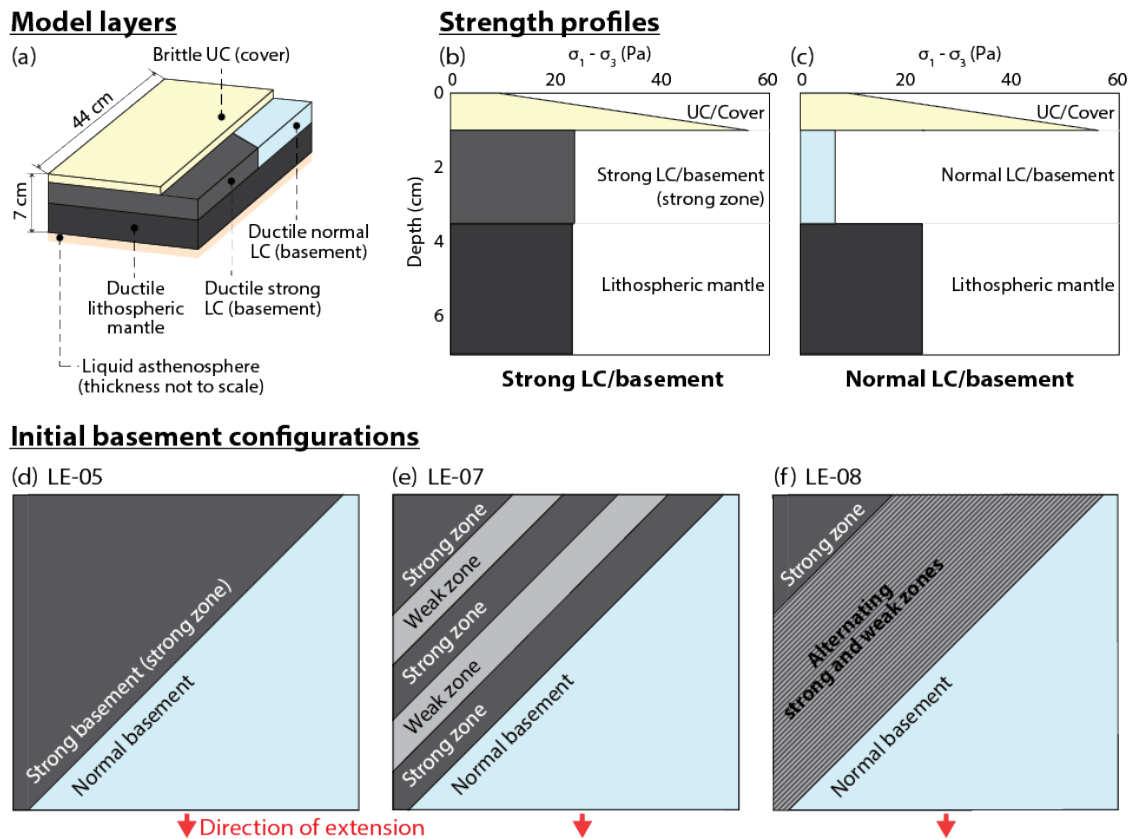
140 **Figure 2** (a) Experimental setup. (b) Oblique view photograph of the model (44 cm long
 141 and 40 cm wide) at the start of the experiment. (c) Top view photograph of the model surface
 142 (Exp LE-05) at the end of the experiment. The dashed line indicates the final geometry of the
 143 strong-normal basement boundary (see Fig. 3 for illustration of basement geometries). In all
 144 figures, the red arrow indicates the direction of extension.

145

146 One side of the model was attached to a moving wall pulled by a linear actuator, imposing an
 147 orthogonal extensional boundary condition that simulates extension similar to that of N-S
 148 rifting between Australia and Antarctica in the Early Cretaceous (Ball et al., 2013; Miller et
 149 al., 2002). Orthogonal extension boundary conditions ensure that the formation of any faults
 150 that are oblique to the extension direction are caused by strength anisotropies in the model
 151 crust, as opposed to imposed kinematic boundary conditions. The ductile basement layer was
 152 made up of a “strong” and “normal” domain (Fig. 3). The geometries and materials within the
 153 strong domain were varied to test their influence on fault patterns in the cover. In Exp LE-01
 154 (the reference experiment) and LE-05, the strong basement was homogeneous. In Exp LE-07
 155 and LE-08, the strong basement was anisotropic, whereby the width of the relatively strong
 156 and weak zones which make up the anisotropy was varied. The viscosity of the ductile
 157 basement material determines the strength of the lithosphere, so that incorporating the
 158 anisotropy in this layer creates zones in the lithosphere which vary in their resistance to

159 deformation (Molnar et al., 2019; Morley, 1999). Widely spaced weak-strong boundaries are
 160 comparable with terrane boundaries, while the narrowly spaced anisotropy represents
 161 penetrative metamorphic fabrics (e.g., foliation). Boundary effects were expected due to
 162 friction between the model's lateral boundaries and the confining U-shaped walls.

163



164

165 **Figure 3** Structure (a) and strength profiles (b-c) of the multi-layer model lithosphere. (d-f)
 166 The configuration of the basement at the start of the experiments. The ductile basement layer
 167 in Exp LE-01 (the reference experiment) has the same geometry as the basement in Exp LE-
 168 05 but is made of less viscous material (equivalent of “weak zone in basement” in Table 1).
 169 The weak zone within the strong basement is only slightly more viscous than the normal
 170 basement material.

171

172 2.2 Scaling and materials

173 Model parameters (e.g., length, mass, time, and velocity) and the mechanical properties of the
 174 chosen analogue materials were scaled down so that deformation occurred within a

175 convenient time period while still behaving consistently with nature (i.e., the prototype)
 176 (Ramberg, 1967). The scaling properties used in the experiments are presented in Table 1.

177

178 **Table 1** Model scaling parameters and material properties. UC = upper crust; LC = lower
 179 crust; ESPH = Envirospheres; PDMS = polydimethylsiloxane; WPL = white Plasticine; BPL
 180 = black Plasticine; K1 = hollow glass microspheres; NS = Natrosol.

181

		Thickness		Density		Viscosity		Material
		Model (mm)	Nature (km)	Model (kg/m ³)	Nature (kg/m ³)	Model (Pa s)	Nature (Pa s)	
Normal crust								
UC (cover)	Brittle	10	10	962	2650	-	-	Sand+ESPH
Normal LC (basement)	Ductile	25	25	980	2700	4.0×10^4	2.0×10^{21}	PDMS
Strong crust								
UC (cover)	Brittle	10	10	962	2650	-	-	Sand+ESPH
Strong zone in LC (basement)	Ductile	25	25	985	2715	5.7×10^5	2.9×10^{22}	PDMS+WPL+K1
Weak zone in LC (basement)	Ductile	25	25	985	2715	7.3×10^4	3.6×10^{21}	PDMS+WPL+K1
Lithospheric mantle	Ductile	35	35	1067	2940	5.9×10^5	3.0×10^{22}	PDMS+BPL+K1
Asthenosphere	Fluid	-	-	1125	3100	380	1.9×10^{19}	NaCl-NS
Scaling factors: model/nature		$L^* = 1 \times 10^{-6}$		$\rho^* = 3.63 \times 10^{-1}$		$\eta^* = 2.0 \times 10^{-17}$		
Time scaling factor		$t^* = \eta^*/(\rho^* \cdot g^* \cdot L^*)$		$t^* = 5.5 \times 10^{-11}$		1 h in model ~ 2.1 Ma in nature		
Velocity scaling factor		$v^* = l^*/t^*$		$v^* = 1.8 \times 10^4$		41 mm/h in model ~ 20 mm/yr in nature		
Gravity scaling factor		$g^* = g_m/g_p$		$g^* = 1$				
Stress scaling factor		$\sigma^* = \rho^* \cdot L^*$		$\sigma^* = 3.63 \times 10^{-7}$				

182

183

184 A length scaling factor $L^* = L_m/L_p = 1 \times 10^{-6}$ was adopted (subscripts m and p refer to the
 185 model and natural prototype, respectively), so that 1 cm in the model represents 10 km in
 186 nature. The 44 cm by 40 cm surface area of the model therefore corresponds to a 440 km \times
 187 400 km area in nature (Fig. 1a). The rate of extension (~ 4.1 cm/hr) scales to ~ 2 cm/yr in
 188 nature, which is comparable to the divergence rate between Australia and Antarctica at ca.
 189 100 Ma (Müller et al., 2016). The experiments ended after ~ 42 % extension, by which time
 190 the models had been extended ~ 18.7 cm. The scaling factor for density ρ^* was set to $3.63 \times$
 191 10^{-1} . The experiments were run under normal gravitational acceleration, so that the scaling
 192 factor for acceleration due to gravity $g^* = 1$, which gives a scaling factor for stress $\sigma^* = \rho^* \times$
 193 $g^* \times L^* = 3.63 \times 10^{-7}$.

194

195

196

For the model cover, a mixture of dry granular materials with a bulk density $\rho_b = \rho_m \approx$
 960 kg/m³ was prepared to approximate a scaled natural density of $\rho_p = 2,650$ kg/m³. We
 used a mixture of dry quartz sand ($\rho_b = 1,580$ kg/m³) and hollow ceramic Envirospheres®

197 BLF and BL150 ($\rho_b \approx 390 \text{ kg/m}^3$) with mass percentages of $\sim 77.9\%$, 21.2% , and 1.9% ,
198 respectively, similar to Molnar et al. (2017). The internal friction angle $\phi < 38^\circ$ and very low
199 cohesion value $c \sim 9 \text{ Pa}$ of this material, measured by Molnar et al. (2017) using a Hubbert-
200 type shear apparatus, makes it a suitable analogue for modelling the brittle cover with a
201 Mohr-Coulomb behavior (e.g., Byerlee, 1978; Davy & Cobbold, 1991; Mandl et al., 1977;
202 Schellart, 2000). The quartz sand is characterized by a homogeneous grain size distribution,
203 with $\sim 73\%$ of the grains falling in the $150\text{--}300 \mu\text{m}$ range.

204 To model the ductile layers, we used polydimethylsiloxane (PDMS), a transparent, high
205 viscosity, high molecular weight silicone polymer. PDMS and PDMS-based mixtures are
206 near-Newtonian fluids frequently used in analogue modeling studies (e.g., Cruden et al.,
207 2006; Molnar et al., 2017, 2018, 2019; Pysklywec & Cruden, 2004; Riller et al., 2012;
208 Weijermars & Schmeling, 1986). Our PDMS (Wacker Elastomer NA) has a density $\rho_m \approx$
209 980 kg/m^3 , which scales to a natural density $\rho_p \approx 2700 \text{ kg/m}^3$.

210 The basement layer is divided into two domains separated by a vertical interface 45° to the
211 extension direction (Fig. 3d–f), consistent with the orientation of the NE-SW boundary and
212 structural trend of the Selwyn Block in the corresponding area in nature (Fig. 1). One domain
213 of “strong” basement approximates the Selwyn Block. The “strong zone” material within the
214 strong basement (Fig. 3) is a mixture of PDMS, modeling clay (white Colorific Plasticine[®]),
215 and 3M[®] K1 hollow glass microspheres (e.g., Cruden et al., 2006; Molnar et al., 2017; Riller
216 et al., 2012). Combining the PDMS with modeling clay increases its effective viscosity and
217 density, while adding glass microspheres reduces its density and increases its effective
218 viscosity. The relative amounts of the three components were adjusted to a mixture with
219 $61.0 \text{ vol}\%$ PDMS, $16.9 \text{ vol}\%$ white Plasticine[®], and $22.1 \text{ vol}\%$ microspheres, giving a density
220 $\rho = 985 \text{ kg/m}^3$ and an effective viscosity of $\sim 5.7 \times 10^5 \text{ Pa s}$ (at our experimental strain rate of
221 $1.0 \times 10^{-4} \text{ s}^{-1}$) and scaling to a natural density of $\rho = 2715 \text{ kg/m}^3$ and natural viscosity of $2.9 \times$
222 10^{22} Pa s . The rheological properties of the PDMS mixture were measured using an Anton
223 Paar Physica MCR-301 parallel plate rheometer. The experimental strain rate was estimated
224 by dividing the velocity of the linear actuator (i.e., the rate at which the model was extended)
225 by the total initial model thickness of 7 cm (Benes & Scott, 1996).

226 The strong zone material is one order of magnitude more viscous than the neighboring
227 “normal” basement domain, which consists of pure PDMS ($\sim 4.0 \times 10^4 \text{ Pa s}$). Anisotropies
228 within the strong basement are reproduced by incorporating linear “weak zones” (Fig. 3)

229 using a PDMS mixture consisting of 80.9 vol% PDMS, 9.0 vol% white Plasticine[®], and
 230 10.1 vol% microspheres. This material has an effective viscosity of $\sim 7.3 \times 10^4$ Pa s, hence it
 231 is only slightly more viscous than the normal basement material.

232 The model lithospheric mantle is a mixture of 55.8 vol% PDMS, 29.7 vol% modeling clay
 233 (black Colorific Plasticine[®]), and 14.6 vol% 3M[®] K1 hollow glass microspheres ($\rho =$
 234 125 kg/m^3). Based on previous analogue modelling of rifting (Molnar et al., 2017), we used a
 235 mixture of 55.8 vol% PDMS, 29.7 vol% black Plasticine[®], and 14.6 vol% microspheres to
 236 achieve a density $\rho_m = 1067 \text{ kg/m}^3$ and effective viscosity of 5.9×10^5 Pa s, corresponding to
 237 an upscaled density $\rho_p = 2940 \text{ kg/m}^3$ and viscosity of 3.0×10^{22} Pa s.

238 The model asthenosphere is a mixture of Natrosol[®] 250 HH, NaCl (sodium chloride),
 239 formaldehyde, and deionized water (Boutelier et al., 2016; Molnar et al., 2017). Natrosol[®]
 240 hydroxyethylcellulose is a water-soluble polymer that can be used to modify the viscosity of an
 241 aqueous solution without significantly affecting its density (Boutelier et al., 2016). Natrosol[®]
 242 acts as a Newtonian fluid under shear strain rates typically employed in experimental
 243 tectonics (Boutelier et al., 2016). The model asthenosphere mixture has a viscosity $\mu_m =$
 244 380 Pa s , scaling to a prototype viscosity $\mu_p = 1.9 \times 10^{19} \text{ Pa s}$, which is comparable with
 245 natural viscosity estimates for the asthenosphere (Artyushkov, 1983; Ranalli, 1995). The
 246 mixture has a density $\rho_m = 1,125 \text{ kg/m}^3$ (Molnar et al., 2017), equivalent to a natural density
 247 $\rho_p \approx 3,100 \text{ kg/m}^3$ (e.g., Pysklywec and Cruden, 2004).

248 2.4 Deformation monitoring and analysis

249 Deformation in the cover layer was monitored during the experiment by stereoscopic particle
 250 imaging velocimetry (PIV) (Adam et al., 2005), so that the resulting strain distribution and
 251 fault orientations could be characterized over time. The PIV system comprises three high-
 252 speed cameras that provide a spatial resolution $\geq 1 \text{ mm}$ and a temporal resolution $\geq 0.1 \text{ s}$
 253 (Molnar et al., 2017). Successive images were recorded at 15 s intervals during each
 254 experimental run. Surface strain and topographic data were derived following the workflow of
 255 Molnar et al. (2017). The incremental displacement field was computed using stereo cross
 256 correlation, forming the basis for deriving the strain tensor components,

$$257 \quad E_{ij} = \frac{\partial V_i}{\partial_j} \text{ with } i \in \{x, y, z\} \text{ and } j \in \{x, y, z\}$$

258 where E_{ij} describes the gradient in the vector component i along the j axis (Adam et al.,
 259 2005), and V is the velocity vector. The scalar fields were used to derive incremental normal
 260 and shear strain as well as the height of the model surface, or digital elevation model (DEM).
 261 The cumulative strain was calculated as the sum of the incremental strain and used to produce
 262 a grid of finite strain ellipses. The maximum normal strain on the surface, E_{surf} , was derived
 263 from the larger eigenvalue of the 2D strain matrix

$$264 \quad \begin{vmatrix} E_{xx} & E_{xy} \\ E_{yx} & E_{yy} \end{vmatrix}$$

265 and the relationship

$$266 \quad E_{surf} = \frac{(E_{xx} + E_{yy})}{2} + \sqrt{\frac{(E_{xx} - E_{yy})^2}{4} + \frac{(E_{xy} + E_{yx})^2}{4}}$$

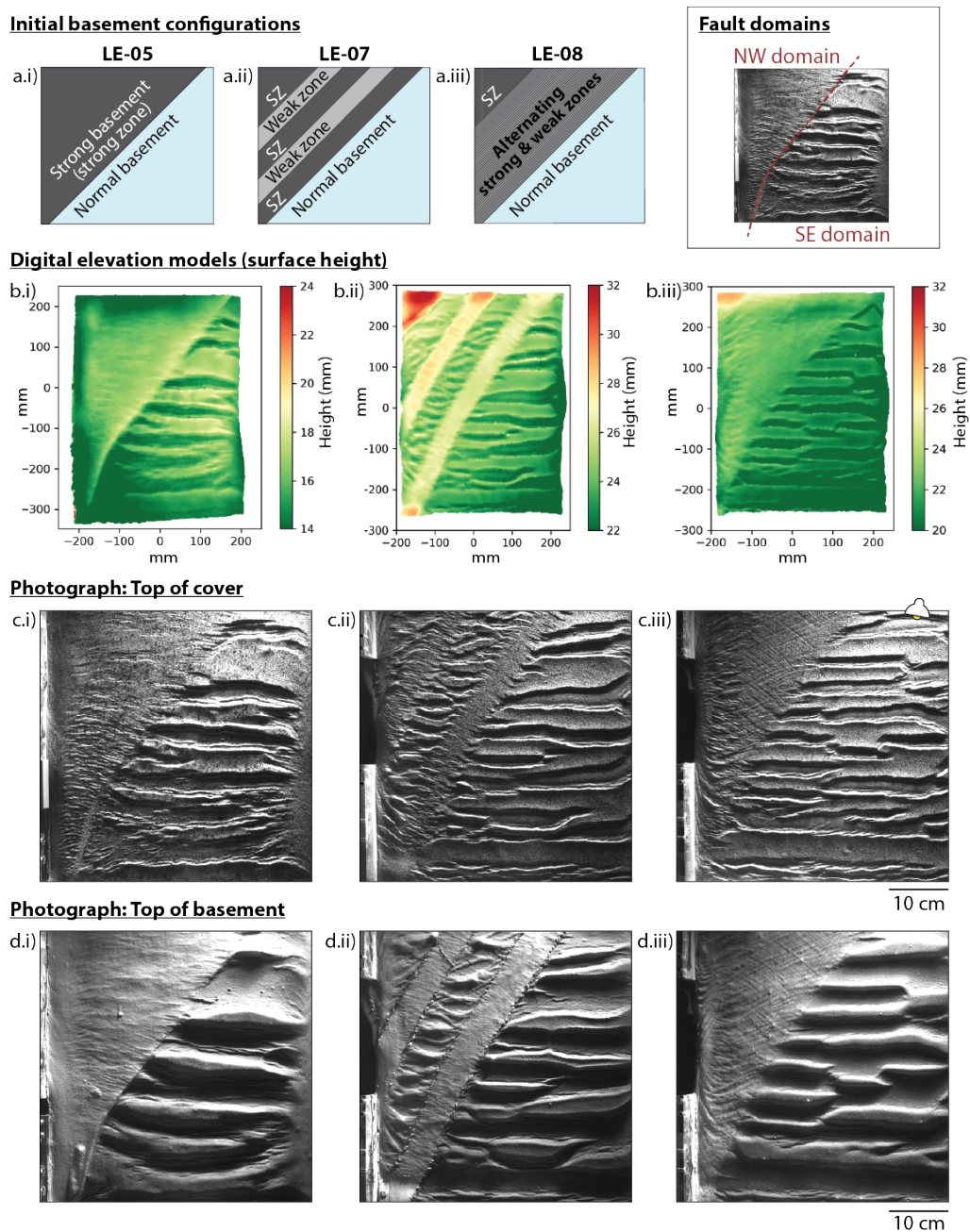
267 A local coordinate system was chosen such that the z -direction is aligned with the surface
 268 normal. E_{xx} and E_{xy} are partial derivatives of the velocity components $\partial V_x/\partial x$ and $\partial V_x/\partial y$,
 269 and E_{yx} and E_{yy} are partial derivatives of the velocity components $\partial V_y/\partial x$ and $\partial V_y/\partial y$. Strain
 270 maps, complemented with DEMs and top-view photographs of the model surface
 271 (illuminated with oblique lighting) enabled us to track the nucleation, growth, and
 272 distribution of faults at different stages of the experiments. The final geometries of the
 273 basement anisotropies were documented by photographing the top surface of the basement
 274 layer after the granular cover material was removed at the end of each experiment.

275

276 3. Results

277 We present the results of four experiments: Exp LE-01, LE-05, LE-07, and LE-08. When
 278 viewing the models in map view, the upper side of the image is referred to as “north”, and the
 279 model is being extended towards the “south”. In describing the fault patterns, the cover is
 280 divided into two domains: a NW domain, underlain by the strong basement (with or without
 281 weak zones), and a SE domain, which overlies the normal basement (Fig. 4). The basement
 282 anisotropies were oriented 45° to the extension direction at the start of the experiment and
 283 underwent progressive rotation towards $\sim 30^\circ$ N by the end of the experiment due to stretching
 284 of the model. Faults near the western and eastern boundaries of the models curve towards
 285 parallelism with the model edges. This boundary effect results from friction between the

286 model's lateral boundaries and the confining U-shaped walls. It affects a small area outside
 287 the central region of interest.



288

289 **Figure 4** Results of orthogonal extension experiments at 4.5 h (47% strain) in map view, with
 290 no anisotropy (a.i), 5.4 cm-wide weak zones (a.ii), and ~2 mm-wide weak zones (a.iii) in the
 291 strong basement block. (b) DEM from photogrammetric PIV data. (c) and (d) are top-view
 292 photographs of the surface of model (cover) and basement, respectively, with oblique
 293 illumination from the top right corner. Larger versions of these photographs are available in
 294 the supporting information (Figures S10 to S15). The top right inset shows the position of the
 295 NW and SE domains. SZ = strong zone.

296 3.1 Reference experiment: quasi-homogeneous basement (Exp LE-01)

297 Our reference experiment (LE-01) resulted in an extension-orthogonal, E-W trending horst
298 and graben system in the cover (Fig. S2 in supporting information). Based on the DEM
299 (Movie S3 in supporting information), E-W trending normal faults began to nucleate by
300 ~ 0.3 h (3% extension). As extension progressed, the faults propagated both westwards and
301 eastwards. They reached their final length at ~ 2 h (21% extension), after which strain was
302 accommodated by widening of the graben.

303 Despite the different compositions of the two basement domains, the viscosity contrast
304 between the strong domain ($\sim 7.3 \times 10^4$ Pa s) and the normal domain ($\sim 4.0 \times 10^4$ Pa s) is
305 negligible, so that the style of faulting across the entire model area is uniform (Fig. S2 in
306 supporting information). At the time of running these experiments, we determined that
307 conducting a second control experiment with a uniform basement was not necessary, as it
308 would have led to the same result as Exp LE-01 (see S2 in supporting information). The
309 results from this experiment suggest that the viscosity contrast between a strong basement
310 and normal basement must be significantly large for two adjoining rheologically different
311 basement domains to influence the orientation of rift faults during extension.

312 3.2 Strong vs. normal basement (Exp LE-05)

313 Exp LE-05 involves a homogeneous strong basement, as in Exp LE-01. However, the strong
314 basement material (with an effective viscosity of $\sim 5.7 \times 10^5$ Pa s) is one order of magnitude
315 more viscous than the adjacent normal basement ($\sim 4.0 \times 10^4$ Pa s). The effect of this strength
316 contrast is apparent in the distinct styles of faulting above the two domains (Fig. 4b.i and
317 4c.i). The SE domain is characterized by an E-W trending horst and graben system. Strain
318 was localized along oppositely dipping faults which formed at early stages (~ 0.8 h; 8%
319 strain) and were spaced ~ 3 to 4 cm apart by the end of the experiment (Movies S4 and S5 in
320 supporting information). The faults reached their final length at ~ 1.3 h (13% strain), when
321 their lateral propagation was arrested at the model boundary and the diagonal strong-normal
322 basement boundary. As extension progressed, the grabens deepened as throw along the
323 bounding faults increased. Once the boundary faults had propagated to the bottom of the
324 cover, strain was accommodated by widening of the graben.

325 In the NW domain, strain in the cover was more distributed, resulting in short, <1 mm-spaced
326 faults (Fig. 4c.i). The faults initially formed in the south (~ 1.4 h; 15% strain) and then began
327 nucleating in the north, near the model center (~ 2.0 h; 21% strain) as extension progressed.

328 By the end of the experiment, faults above the strong basement had not linked together via
329 relay structures, so that their length remained shorter than the faults in the SE domain (Fig.
330 4c.i). Most of the faults in the NW domain are E-W, but those within ~30 mm of the strong-
331 normal basement boundary trend WNW-ESE, curving to approach perpendicularity to the
332 boundary.

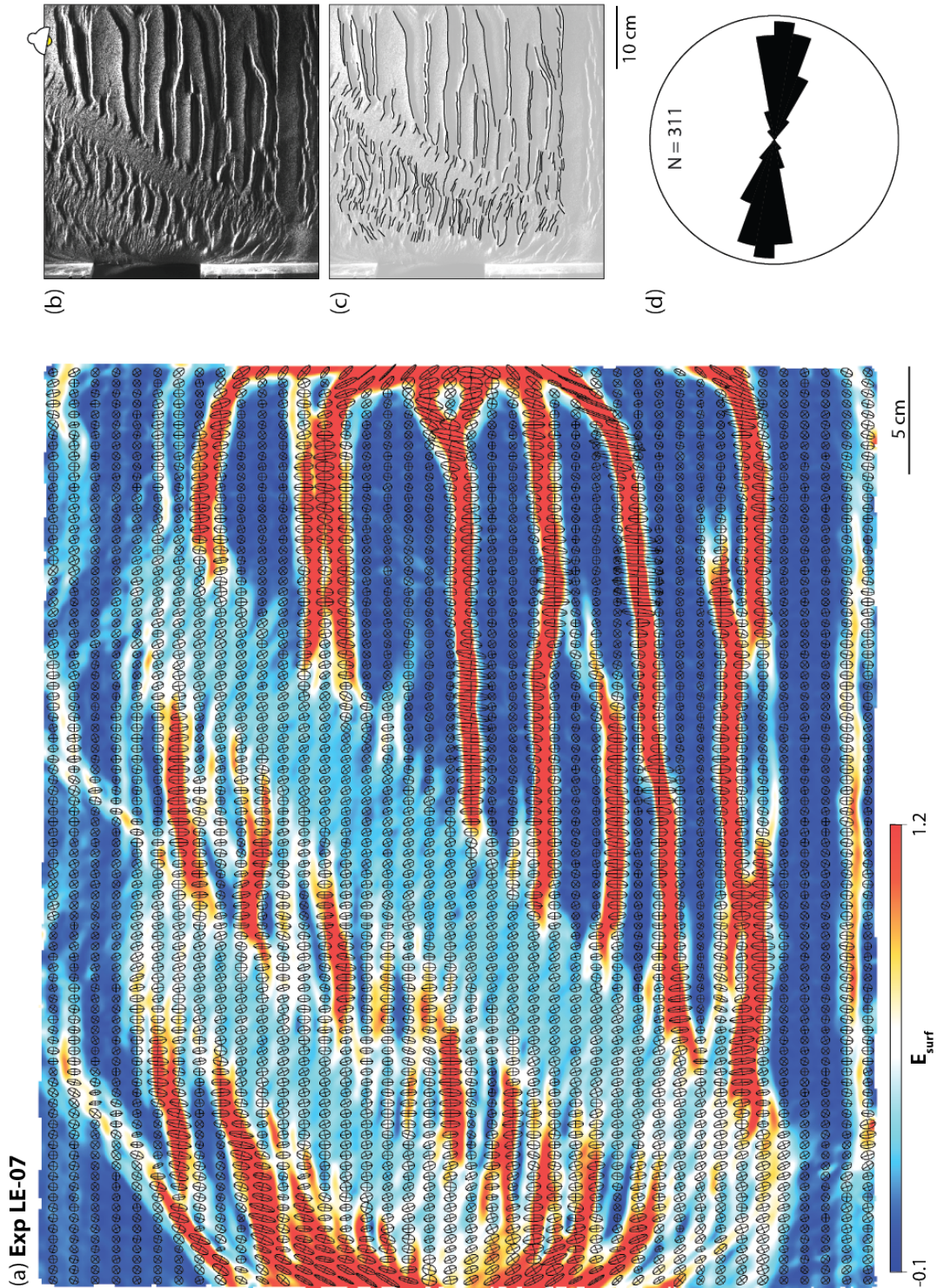
333 3.3 Wide anisotropy in the strong basement (Exp LE-07)

334 The overall evolution and final pattern of faults in the SE domain in Exp LE-07 and LE-08
335 (Section 3.4) are very similar to the horst-and-graben style of faulting in the SE domain of
336 Exp LE-05. In Exp LE-07, the fault pattern in the NW domain is influenced by the presence
337 of two linear weak zones which are 5.4 cm wide and spaced 5.4 cm apart (Fig. 4a.ii and
338 5b.ii). Faults above the weak zones form grabens bound by oppositely dipping, E-W trending
339 faults, comparable to the style of faulting in the SE domain (Fig. 4c.ii). The spacing of these
340 faults appears to be intermediate between two end members of fault localization (i.e., highest
341 degree of localization above the normal basement and even distribution above the strong
342 basement). NW-SE trending faults above the strong basement are evenly distributed and
343 narrowly spaced.

344 In the top view photographs of the model surface (Movie S6 in supporting information), E-W
345 trending faults in the SE domain had begun forming by ~0.8 h (8% strain). E-W trending
346 faults above the weak zones within the NW domain began forming at ~1.1 h (11% strain).
347 Faults above strong zones within the NW domain began forming at ~2.0 h (21% strain), first
348 nucleating at the boundaries of the weak zones and then propagating inwards, orthogonal to
349 the basement domain boundaries.

350 The formation of NW-SE trending faults above the strong zones and E-W trending faults
351 above the weak zones within the NW domain were controlled by the widely spaced
352 anisotropy in the underlying basement (Fig. 5). This experiment demonstrates that strain
353 partitioning resulted from the presence of extension-oblique zones of highly contrasting
354 strengths, simulated by large viscosity differences in the models. Finite strain ellipses at the
355 end of this experiment exhibit a N-S maximum stretching direction in the SE domain and
356 weak zones in the NW domain (consistent with the imposed N-S extension) and a NNW-SSE
357 maximum stretching direction above the strong basement in the NW domain (Fig. 5a).

358



359

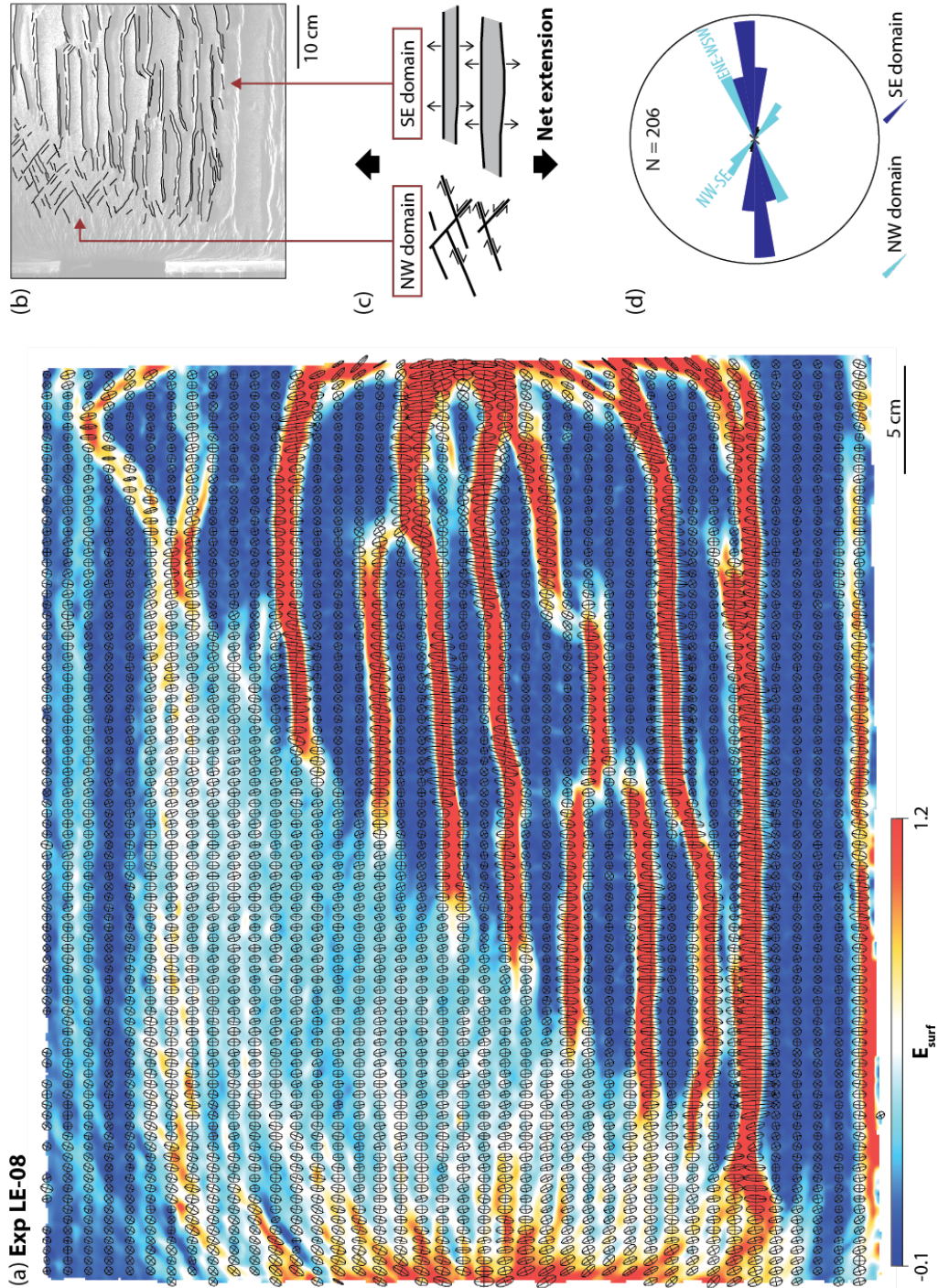
360 **Figure 5** Results from Exp LE-07: (a) cumulative maximum normal strain on surface and 2D
 361 strain ellipses at the end of the experiment, plotted at their initial location ($t = 0$); (b) top view
 362 photograph of model surface illuminated at an angle from the north, indicated by the lamp on
 363 the figure; (c) fault traces interpreted from photograph of model surface; and (d) rose diagram
 364 of fault traces. Note rotation of fault orientation at the boundaries between weak and strong
 365 zones. For the evolution of the cumulative strain, see Movie S7 in the supporting information.

366 3.4 Narrow anisotropy in the strong basement (Exp LE-08)

367 In Exp LE-08, we implemented a higher degree of anisotropy than in Exp LE-07 by creating
368 narrowly spaced, ~2 mm-wide weak zones within the strong basement, separated by ~2 mm-
369 wide strong basement material (Fig. 4a.iii). In the top view photographs of the model surface
370 (Movie S8 in supporting information), E-W trending faults in the SE domain began forming
371 by ~0.8 h (8% strain). Faults in the NW domain began forming at ~1.4 h (15% strain) near
372 the model's western edge. Two sets of narrowly spaced faults, trending NW-SE and ENE-
373 WSW, began forming at ~3.1 h (32% strain) (Fig. 6b). These coeval fault sets are oblique to
374 the N-S extension direction, the NE-SW trending anisotropy, and the strong-normal basement
375 boundary. The two sets form an apparently conjugate or orthorhombic pattern, with an acute
376 bisector trending WNW-ESE (100°) (Fig. 7b). The obtuse bisector trends NNE-SSW (10°),
377 deviating slightly from the imposed N-S extension. The ENE-WSW trending set is more
378 pronounced than the WNW-ESE trending set because they exhibit greater dip-slip
379 displacement. Finite strain ellipses at the end of this experiment exhibit a N-S maximum
380 stretching direction in the SE domain and a NNW-SSE maximum stretching direction in the
381 NW domain (Fig. 6a).

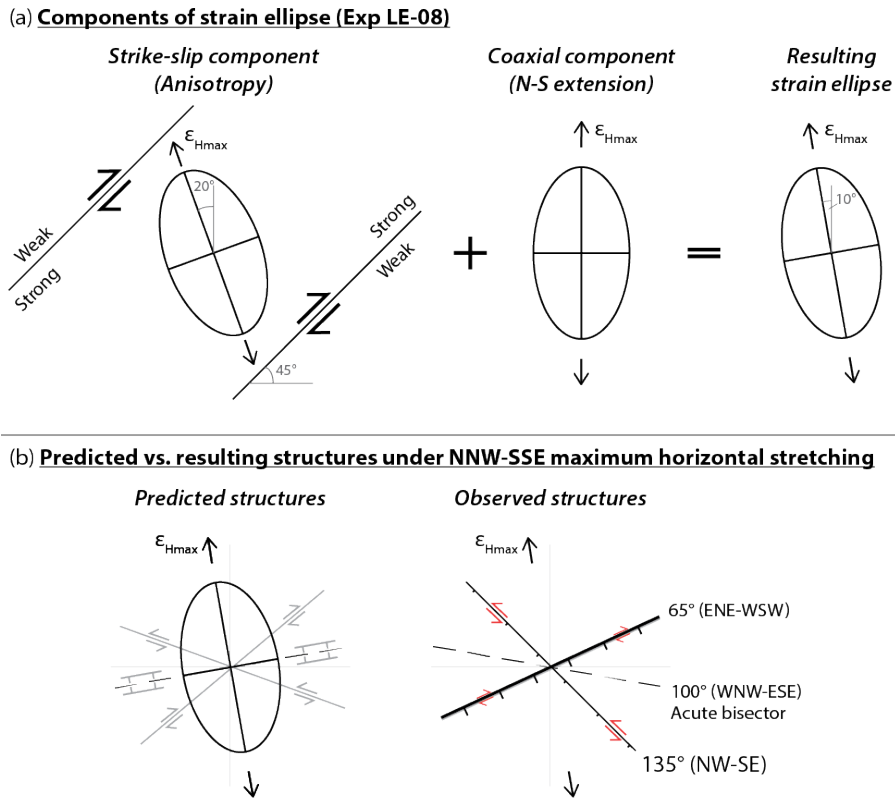
382 Although the fault populations in the NW and SE domains exhibit different orientations, both
383 patterns formed as products of the same imposed N-S directed bulk extension (Fig. 6b and
384 6c). Parallel, E-W trending faults in the SE domain represent extension-orthogonal normal
385 faults that are consistent with formation in an Andersonian normal faulting regime. In
386 contrast, the orthorhombic fault pattern in the NW domain signifies a local change in the 3D
387 strain field due to the role of the penetrative anisotropy in the basement. Because these faults
388 must accommodate the bulk N-S extension, we infer that these oblique fault sets must have a
389 strike-slip component, as indicated in Fig. 6c and 7b.

390



391

392 **Figure 6** Results from Exp LE-08: (a) cumulative maximum normal strain on surface and 2D
 393 strain ellipses at the end of the experiment, plotted at their initial location ($t = 0$); (b) fault
 394 traces overlain on top-down photograph of model surface, (c) schematic plan view illustration
 395 of the accommodation of N-S extension by an orthorhombic fault set in the NW domain and
 396 E-W faults in the SE domain, and (d) rose diagram of fault traces. For the evolution of the
 397 cumulative strain, see Movie S9 in the supporting information.



398

399 **Figure 7** Schematic illustration of deformation and associated kinematics in the NW domain
 400 of Exp LE-08. (a) The representative strain ellipse can be broken down into a strike-slip (non-
 401 coaxial) and coaxial component. These representative 2D strain ellipses are not to scale; the
 402 relative contributions of the strike-slip and coaxial component may be different in the
 403 experiment. (b) Comparing the predicted structures (under a NNW-SSE maximum horizontal
 404 stretching direction ϵ_{Hmax}) with the resulting faults at the model surface at the end of the
 405 experiment. The reason for this discrepancy is an effect unaccounted for in the simple
 406 prediction (see Section 4.3 for explanation). The observed ENE-WSW trending faults are wider
 407 than NW-SE faults, suggesting that they have accommodated a significant amount of dip-slip
 408 displacement (greater than strike-slip displacement).

409

410 **4. Discussion**

411 In the experiments, deformation in the cover was influenced by re-orientation of the stress
 412 and strain fields across the ductile basement layer, as there were no weak layers that
 413 separated the cover and basement materials (cf. "attached stress regime" in Bell, 1996). As a
 414 result, faults in the brittle cover were localized above areas of thinning in the ductile
 415 basement (compare Fig. 4c and 4d).

416 4.1 The influence of basement strength on fault spacing

417 Stronger basement domains in our models correspond with distributed deformation in the
418 overlying cover, while weaker basement domains correspond to localized deformation. In
419 Exp LE-05, the NW domain (above the strong basement) is populated by short, closely
420 spaced faults. The SE domain (above the normal basement) experienced a higher degree of
421 strain localization, evidenced by widely spaced grabens that are bounded by long faults with
422 large displacements (Fig. 4c.i). Similarly in Exp LE-07, the spacing of faults in the NW
423 domain above the weak zones is greater than between faults above the strong zones, but
424 smaller than the spacing between faults in the SE domain (Fig. 4c.ii). These results suggest
425 that fault spacing is controlled by the strength ratio between the ductile and brittle layers
426 (Davy et al., 1995), which is modulated by the viscosity of the ductile basement material.

427 Our findings are in agreement with previous work on brittle-ductile coupling, which
428 describes the interaction between viscous flow and brittle failure at the horizontal interface
429 between brittle and ductile layers in the continental lithosphere (Ranalli, 1995). The
430 mechanical role of the ductile layer in determining the transition from localized to distributed
431 brittle deformation has been investigated through numerous numerical and analogue
432 experiments of compressional (Riller et al., 2012; Schueller et al., 2005, 2010; Schueller &
433 Davy, 2008) and extensional systems (Bellahsen et al., 2003; Brun, 1999; Sharples et al.,
434 2015; Wijns et al., 2005).

435 4.2 Rotation of strain axes above a strong, anisotropic basement block

436 Despite the orthogonal extension boundary condition in our experiments, our models simulate
437 transtension due to the presence of NE-SW trending anisotropies in the basement. The
438 deformation observed in the brittle cover reflects deformation in the underlying basement,
439 which is governed by ductile flow (Fossen & Tikoff, 1998). The obliquity of faults in the NW
440 domain of Exp LE-07 and LE-08 suggests that the model cover did not experience pure shear
441 during extension. Although extension-oblique faults in the NW domain form a small subset
442 of the total fault population, we discuss them at length because their nature reflects the
443 influence of different geometries of basement anisotropies (compare Exp LE-07 and LE-08;
444 Fig. 4).

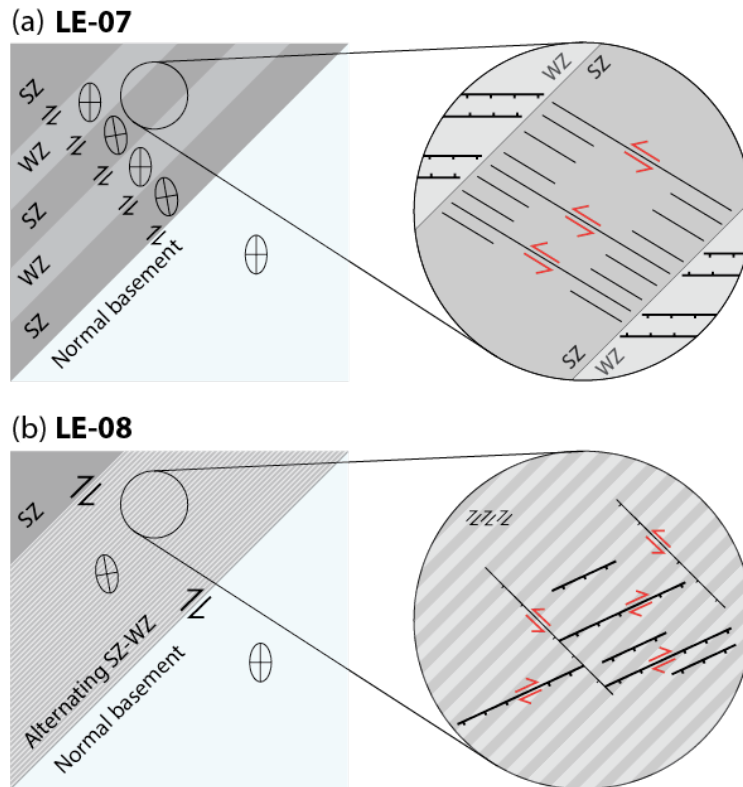
445 Calculated finite strain ellipses at the end of Exp LE-08 (Fig. 6a) exhibit a N-S maximum
446 stretching direction ϵ_{Hmax} in the SE domain. The NW domain is populated by strain ellipses
447 with a NNW-SSE ϵ_{Hmax} , deviating slightly from N-S. We can explain the rotation of the 2D

448 strain ellipses from N-S to NNW-SSE by the superposition of a coaxial strain component (the
449 N-S imposed extension) and a strike-slip component (Fig. 7a).

450 For the strike-slip component, we can infer dextral shearing along each strong-weak interface
451 in the basement, as the anisotropies rotated from 45° to $\sim 30^\circ$ N with increasing extension (Fig.
452 4). As shown in Fig. 7a and 8, dextral motion along strong-weak interfaces results in internal
453 sinistral shearing within each narrow strong zone, consistent with the anti-clockwise rotation
454 of the strain ellipses. This same strain ellipse rotation is also demonstrated in Exp LE-07
455 within each strong zone in the NW domain (Fig. 5a).

456 From the NNW-SSE trending ϵ_{Hmax} , we expected ENE-WSW trending normal faults or a
457 conjugate set of faults with an ENE-WSW trending acute bisector to form in the NW domain
458 (Fig. 7b). Instead, strain in this domain is accommodated by an orthorhombic fault system,
459 where the ENE-WSW set is dominant. We infer that the ENE-WSW faults have a significant
460 dip-slip and minor strike-slip offsets. A less dominant NW-SE fault set with a significant
461 strike-slip component and a minor dip-slip component must also form to maintain strain
462 compatibility (e.g., Fossen & Tikoff, 1998). The reason for the discrepancy between the
463 observed and predicted fault patterns is outlined in detail in Section 4.3.

464 The presence of alternating 5.4 cm-wide strong and weak zones in the NW domain of Exp
465 LE-07 resulted in strain partitioning. ϵ_{Hmax} trends N-S above the weak zones within the NW
466 domain (Fig. 5), resulting in E-W trending faults. The NNW-SSE trending ϵ_{Hmax} is confined
467 to the strong zones. In this experiment, E-W trending faults first nucleated and propagated in
468 the SE domain and in the weak zones of the NW domain until they reached the interfaces
469 with the strong zones; NW-SE trending faults then propagated from the interfaces and into
470 the center of the strong zones. We interpret that the strong zones acted as transfer zones (cf.
471 Zwaan and Schreurs, 2017), across which older faults in the SE domain and in the NW
472 domain weak zones linked up via extension-oblique faults (Fig. 8a). To maintain strain
473 compatibility, these NW-SE trending faults are likely to have a sinistral strike-slip
474 component. The change in structural style of faults as they propagate laterally from the weak
475 to strong zones is comparable with observations from seismic reflection data from the Great
476 South Basin, New Zealand (Phillips & McCaffrey, 2019). Here, a strong granitic laccolith
477 appears to inhibit the propagation of extension-orthogonal normal faults from the
478 sedimentary unit, causing the fault system to splay before reaching the boundary between the
479 mechanically contrasting units.



480

481 **Figure 8** (a) Strain partitioning in the NW domain of Exp LE-07. The 2D strain ellipses
 482 reflect N-S maximum horizontal stretching in the normal basement and in the weak zones
 483 within the strong basement. In the strong zones, they are rotated anticlockwise. (b) Strike-slip
 484 movement along all strong-weak interfaces in the NW domain of Exp LE-08 results in an
 485 “averaging effect” of the anisotropic properties of the basement. Hence the strain ellipse is
 486 rotated anticlockwise across the entire NW domain. SZ= strong zone; WZ = weak zone.

487

488 Strain re-orientation has been observed in lithospheric-scale analogue models where a single
 489 pre-existing weakness in the ductile lower crust has an obliquity up to 45° relative to the
 490 imposed extension (Philippon et al., 2015). In these models, faults in the brittle upper crust
 491 above the strong-weak interface (i.e., so-called “border faults”) exhibit dip-slip kinematics
 492 even though their trends are oblique to the extension direction. Re-orientation of the
 493 extension direction is not apparent for obliquities greater than 45° , and thus strain re-
 494 orientation plays a smaller role in fault pattern development, as faults display predominantly
 495 oblique-slip kinematics (Agostini et al., 2009). According to Philippon and Corti (2016), the
 496 proposed 45° obliquity threshold which determines either strain re-orientation or partitioning
 497 must be investigated further. They also noted that the strain re-orientation/partitioning

498 threshold could be controlled by the initial width of the pre-existing weakness. Our
499 experiments, in which all of the basement anisotropies had an initial 45° orientation, confirm
500 that strain re-orientation and partitioning are modulated by the width and spacing of the
501 anisotropies, which we discuss in the next section. However, our models also generated fault
502 patterns and kinematics that differ from previous models (e.g., Agostini et al., 2009; Corti et
503 al., 2013; Philippon et al., 2015; Philippon & Corti, 2016) as we embedded multiple weak
504 zones in the ductile layer to simulate a penetrative fabric (cf. Morley, 1999).

505 4.3 The scale-dependent role of basement anisotropies on fault patterns

506 The different characteristics of extension-oblique faults in Exp LE-07 (above the strong zones
507 in the NW domain) and LE-08 are attributed to the geometry of the basement anisotropies,
508 which interacted with the imposed boundary conditions. While certain structures would have
509 been expected given the NNW-SSE maximum horizontal stretching (Fig. 7b), the role,
510 kinematics and intensity of faults above the different strong and weak regions were modified
511 by: (i) the 45° angle between the imposed N-S stretching and the boundaries between strong
512 and weak zones, along which local strike-slip movement occurred (Fig. 8), and (ii) the
513 spacing and width of the alternating strong and weak zones. This geometric influence is
514 exemplified by faults in the NW domain of Exp LE-07 (Fig. 5). Here, E-W trending faults
515 above the weak zones forced the dominance of NW-SE trending transfer faults above the
516 strong zones, which link the E-W faults and accommodate extensional strain.

517 Exp LE-07 and LE-08 represent two end-member scenarios where either: a) strain is
518 partitioned between zones of contrasting strength within an anisotropic basement block (Fig.
519 8a), or b) the properties of zones of contrasting strength are “averaged” (Fig. 8b). Exp LE-08
520 demonstrates that a basement block, with a stronger average viscosity than the adjacent block
521 and containing a vertically layered, closely spaced, and penetrative anisotropy, will behave as
522 a single block (Fig. 8b). When the width of the alternating weak and strong zones is below a
523 certain threshold, rotation of the strain axes occurs not just at the strong-weak zone interfaces,
524 but across the entire NW domain. When the width of the anisotropy is increased, alternating
525 weak and strong zones within the strong basement act as discrete basement blocks with their
526 own distinct mechanical properties. Quantifying the threshold width of the anisotropies is
527 beyond the scope of this study, but it is likely to be controlled by the viscosity ratio between
528 the strong and weak zones, the ratio between the brittle crust thickness and the width of the
529 anisotropy, and the minimum resolvable fault displacement in the experimental setup.

530 4.4 Model limitations and implications for natural rift basins

531 Our simplified experiments show that localized strain re-orientation above an anisotropic
532 basement, oblique to the extension direction, is responsible for complex fault patterns in the
533 cover. They also demonstrate that a sufficiently anisotropic basement creates transtension,
534 leading to non-Andersonian, extension-oblique faulting. Here we draw comparisons to the
535 natural case of the Gippsland Basin, which inspired our model design, and discuss the
536 potential contributions of our work to understanding structural inheritance in other rift basins.

537 The starting point for our experimental setup was the enigmatic pattern of Early Cretaceous
538 syn-rift faulting across the Gippsland Basin, attributed to an anomalously strong,
539 heterogeneous, anisotropic lower crustal block (i.e., the Selwyn Block; Cayley et al., 2002;
540 Moore et al., 2016)). The influence of the Selwyn Block is evident in the eastern Otway
541 Basin and western Gippsland Basin, where NE-SW to ENE-WSW trending Early Cretaceous
542 faults are present in the overlying cover (Constantine, 2001; Moore et al., 2000; Norvick &
543 Smith, 2001; Samsu et al., 2019; Willcox et al., 1992) (Fig. 1). This fault set is oblique to the
544 inferred N-S or NNE-SSW direction of regional extension (e.g., Etheridge et al., 1985; Miller
545 et al., 2002; Willcox and Stagg, 1990). It is also oblique to E-W trending orthogonal rift
546 faults that typify areas beyond the boundaries of the Selwyn Block (Fig. 1b). Power et al.
547 (2001, 2003) attributed this obliquity to transtension arising from NNW-SSE directed oblique
548 extension in the Early Cretaceous, based on seismic reflection data from the eastern
549 (offshore) Gippsland Basin (Fig. 1b). Samsu et al. (2019, 2020) used field observations and
550 potential field geophysical data from the western onshore Gippsland Basin to determine that
551 NE-SW to ENE-WSW syn-rift faults are at acute angles to a strong, subvertical NNE-SSW
552 trending fabric in Paleozoic basement rocks of the Melbourne Zone and the NE-SW
553 structural grain of the Selwyn Block (Moore et al., 2016). Our experiments suggest that while
554 transtension could account for the obliquity of some of the faults in the Gippsland Basin, it
555 may reflect the influence of Melbourne Zone or Selwyn Block basement fabrics on fault
556 kinematics. From Exp LE-05 and LE-08, we also deduced that it is the penetrative fabric
557 within an anomalously strong basement block, and not the lateral boundary between strong
558 and normal basement, which likely produced extension-oblique rift faults across a wide area
559 (Fig. 1 and 4).

560 The experimental results do not fully replicate fault patterns in the Gippsland Basin. For
561 instance, basin-scale (>1 km long) ENE-WSW trending normal faults in the western onshore

562 Gippsland Basin (Samsu et al., 2019) are comparable to ENE-WSW trending faults in the
563 NW domain of Exp LE-08. However, this part of the model also contains NW-SE trending
564 faults which are not represented in the basin-scale fault map (Fig. 1). Given the imposed N-S
565 bulk extension in the experiment, strain compatibility required the development of the NW-
566 SE trending conjugate fault set once the ENE-WSW trending faults formed. If such NW-SE
567 faults were present in the Gippsland Basin, their strike-slip and dip-slip displacement may
568 have been too small to generate gravity and magnetic anomalies.

569 The Gippsland Basin could have been exposed to other boundary conditions, such as oblique
570 rifting and an extension direction that is not exactly N-S. Different degrees of rheological
571 contrasts and reactivation of pre-existing faults in the Melbourne Zone and Selwyn Block
572 basement units may have also influenced faulting. Finally, the brittle cover in the natural case
573 is heterogeneous, unlike the homogeneous cover in our models. All of these added
574 complexities in nature would have resulted in fault patterns that are different from those in
575 our experiments.

576 Despite the simplicity of our experiments, they provide insight as to how an underlying,
577 penetrative basement anisotropy could generate extension-oblique faults. The results differ
578 from the more widely explored reactivation of crustal weaknesses (e.g., Autin et al., 2013;
579 Bellahsen and Daniel, 2005; Corti, 2004; Faccenna et al., 1995; Henza et al., 2011, 2010).
580 They also show that oblique kinematics (Withjack & Jamison, 1986) are not necessarily
581 required to form extension-oblique faults. All that is needed is a basement that is sufficiently
582 anisotropic, and this anisotropy does not have to occur at the whole of lithosphere scale (cf.
583 Agostini et al., 2009; Brune et al., 2017; Corti, 2008). Our findings support the statement that
584 the local strain direction indicated by individual faults need not reflect the orthogonal
585 extension boundary condition, as previously shown by Philippon et al. (2015).

586 The influence of basement anisotropies on local strain re-orientation has implications for
587 understanding complex fault systems within transfer zones, where far-field extension vectors
588 and pre-existing basement anisotropies are likely to be oblique (Wilson et al., 2010).

589 Reactivation of basement structures often play a role in the development of transfer zones
590 (Daly et al., 1989; Morfley et al., 2004), and this was thought to be the case in the North
591 Coast Transfer Zone (NCTZ), Scotland. However, Wilson et al. (2010) noted that evidence
592 for reactivation is not as prevalent in the onshore areas of the NCTZ as had been previously
593 implied (Holdsworth, 1989; Roberts & Holdsworth, 1999). Wilson et al. (2010) also showed

594 that fault patterns change across regions with different orientations of pre-existing basement
595 fabrics and that these are oblique to the far-field extension direction. Variations in fault
596 orientations were attributed to a subtle basement influence that generated localized changes in
597 3D transtensional strains. Our experiments support this hypothesis by showing that local
598 extension directions are re-oriented from the far-field extension direction when the basin is
599 underlain by different anisotropic basement domains. This is the case even when the
600 basement fabrics themselves are not reactivated. While previous analogue experiments have
601 provided insight into the influence of a single basement weakness on the formation,
602 geometry, and orientation of transfer zones (e.g., Acocella et al., 1999; Zwaan & Schreurs,
603 2017), pervasive anisotropies should be incorporated into the basement to model complex,
604 basin-scale fault systems within transfer zones (Morley, 1999).

605 Future experiments may require the use of finer-grained granular material to represent the
606 cover and higher resolution particle tracking to enable direct observation of fault kinematics
607 (cf. Philippon et al., 2015). Such a setup would allow us to make direct comparisons with
608 observed fault kinematics in the natural setting. Our models also used a ductile layer to model
609 “basement” anisotropies. In contrast, basement rocks in nature could have anisotropies that
610 formed during ductile deformation but have entered the brittle regime by the time rifting
611 occurred. There are practical challenges with introducing anisotropies in brittle material, but
612 it is worth considering to understand how a brittle anisotropic basement would influence rift
613 faulting in the cover.

614

615 **5. Conclusions**

616 The experimental results presented here describe the control of crustal strength on fault
617 spacing and the length scale-dependent relationship between penetrative basement
618 anisotropies and fault behavior in the cover during a single phase of rifting. How lateral
619 strength anisotropies in the basement influence fault orientations in the cover is a function of:
620 (i) scale (i.e., the width and spacing of anisotropies relative to the size of the modelled area),
621 and (ii) the mechanical properties of the individual zones that make up the anisotropic
622 material. Hence the geometry of basement domains of differing strengths may interact with
623 rift kinematics, impacting the orientation, kinematics, and spacing of faults in the overlying
624 sedimentary basin. We show that the basement of a rift basin must be sufficiently anisotropic
625 for extension-oblique rift faults to form across a wide area. Additionally, such faults can form

626 oblique to the trend of pre-existing basement anisotropies, demonstrating that pre-existing
627 basement structures/weaknesses can be inherited via a mechanism other than reactivation,
628 which would otherwise result in new faults that are parallel to these basement structures.

629

630 **Acknowledgments**

631 The authors thank Steven Micklethwaite for helpful discussions during the preparation of this
632 manuscript. Alexander Peace and two anonymous reviewers are also thanked for constructive
633 reviews. AS was supported by a Monash University Faculty of Science Dean's International
634 Postgraduate Research Scholarship and Postgraduate Publication Award. Data used for this
635 contribution is publicly available at <https://doi.org/10.26180/14027243> (Samsu et al., 2021).

636

637 **References**

638 Acocella, V., Faccenna, C., Funicello, R., & Rossetti, F. (1999). Sand-box modelling of
639 basement-controlled transfer zones in extensional domains. *Terra Nova*, *11*(4), 149–156.
640 <https://doi.org/10.1046/j.1365-3121.1999.00238.x>

641 Adam, J., Urai, J. L., Wieneke, B., Oncken, O., Pfeiffer, K., Kukowski, N., et al. (2005).
642 Shear localisation and strain distribution during tectonic faulting—new insights from
643 granular-flow experiments and high-resolution optical image correlation techniques.
644 *Journal of Structural Geology*, *27*(2), 283–301.
645 <https://doi.org/10.1016/j.jsg.2004.08.008>

646 Agostini, A., Corti, G., Zeoli, A., & Mulugeta, G. (2009). Evolution, pattern, and partitioning
647 of deformation during oblique continental rifting: Inferences from lithospheric-scale
648 centrifuge models. *Geochemistry, Geophysics, Geosystems*, *10*(11).
649 <https://doi.org/10.1029/2009GC002676>

650 Artyushkov, E. V. (1983). *Geodynamics*. Amsterdam: Elsevier.

651 Autin, J., Bellahsen, N., Leroy, S., Husson, L., Beslier, M. O., & D'Acromont, E. (2013). The
652 role of structural inheritance in oblique rifting: Insights from analogue models and
653 application to the Gulf of Aden. *Tectonophysics*, *607*, 51–64.
654 <https://doi.org/10.1016/j.tecto.2013.05.041>

- 655 Ball, P., Eagles, G., Ebinger, C., McClay, K., & Totterdell, J. (2013). The spatial and
656 temporal evolution of strain during the separation of Australia and Antarctica.
657 *Geochemistry, Geophysics, Geosystems*, 14(8), 2771–2799.
658 <https://doi.org/10.1002/ggge.20160>
- 659 Beacom, L. E., Holdsworth, R. E., McCaffrey, K. J. W., & Anderson, T. B. (2001). A
660 quantitative study of the influence of pre-existing compositional and fabric
661 heterogeneities upon fracture-zone development during basement reactivation.
662 *Geological Society, London, Special Publications*, 186(1), 195–211.
663 <https://doi.org/10.1144/gsl.sp.2001.186.01.12>
- 664 Bell, J. S. (1996). Petro geoscience 2. In situ stresses in sedimentary rocks (part 2):
665 Applications of stress measurements. *Geoscience Canada*.
- 666 Bellahsen, N., & Daniel, J. M. (2005). Fault reactivation control on normal fault growth: An
667 experimental study. *Journal of Structural Geology*, 27(4), 769–780.
668 <https://doi.org/10.1016/j.jsg.2004.12.003>
- 669 Bellahsen, N., Daniel, J. M., Bollinger, L., & Burov, E. (2003). Influence of viscous layers on
670 the growth of normal faults: Insights from experimental and numerical models. *Journal*
671 *of Structural Geology*, 25(9), 1471–1485. [https://doi.org/10.1016/S0191-](https://doi.org/10.1016/S0191-8141(02)00185-2)
672 [8141\(02\)00185-2](https://doi.org/10.1016/S0191-8141(02)00185-2)
- 673 Benes, V., & Scott, S. D. (1996). Oblique rifting in the Havre Trough and its propagation into
674 the continental margin of New Zealand: Comparison with analogue experiments. *Marine*
675 *Geophysical Research*, 18(2–4), 189–201. <https://doi.org/10.1007/BF00286077>
- 676 Bird, P. C., Cartwright, J. A., & Davies, T. L. (2014). Basement reactivation in the
677 development of rift basins: an example of reactivated Caledonide structures in the West
678 Orkney Basin. *Journal of the Geological Society*, 172, 77–85.
679 <https://doi.org/10.1144/jgs2013-098>
- 680 Bonini, L., Basili, R., Toscani, G., Burrato, P., Seno, S., & Valensise, G. (2015). The role of
681 pre-existing discontinuities in the development of extensional faults: An analog
682 modeling perspective. *Journal of Structural Geology*, 74, 145–158.
683 <https://doi.org/10.1016/j.jsg.2015.03.004>
- 684 Boutelier, D., Cruden, A., & Saumur, B. (2016). Density and visco-elasticity of Natrosol 250

- 685 HH solutions: Determining their suitability for experimental tectonics. *Journal of*
686 *Structural Geology*, 86, 153–165. <https://doi.org/10.1016/j.jsg.2016.03.001>
- 687 Brun, J. P. (1999). Narrow rifts versus wide rifts: Inferences for the mechanics of rifting from
688 laboratory experiments. *Philosophical Transactions of the Royal Society A:*
689 *Mathematical, Physical and Engineering Sciences*, 357(1753), 695–712.
690 <https://doi.org/10.1098/rsta.1999.0349>
- 691 Brune, S., Corti, G., & Ranalli, G. (2017). Controls of inherited lithospheric heterogeneity on
692 rift linkage: Numerical and analogue models of interaction between the Kenyan and
693 Ethiopian rifts across the Turkana depression. *Tectonics*, 1–20.
694 <https://doi.org/10.1002/2017TC004739>
- 695 Byerlee, J. (1978). Friction of rocks. *Pure and Applied Geophysics*, 116(4–5), 615–626.
696 <https://doi.org/10.1007/BF00876528>
- 697 Cayley, R. A., Taylor, D. H., VandenBerg, A. H. M., & Moore, D. H. (2002). Proterozoic -
698 Early Palaeozoic rocks and the Tyennan Orogeny in central Victoria: The Selwyn Block
699 and its tectonic implications. *Australian Journal of Earth Sciences*, 49(2), 225–254.
700 <https://doi.org/10.1046/j.1440-0952.2002.00921.x>
- 701 Chattopadhyay, A., & Chakra, M. (2013). Influence of pre-existing pervasive fabrics on fault
702 patterns during orthogonal and oblique rifting: An experimental approach. *Marine and*
703 *Petroleum Geology*, 39(1), 74–91. <https://doi.org/10.1016/j.marpetgeo.2012.09.009>
- 704 Collanega, L., Siuda, K., A.-L. Jackson, C., Bell, R. E., Coleman, A. J., Lenhart, A., et al.
705 (2019). Normal fault growth influenced by basement fabrics: The importance of
706 preferential nucleation from pre-existing structures. *Basin Research*, 31(4), 659–687.
707 <https://doi.org/10.1111/bre.12327>
- 708 Constantine, A. (2001). *Sedimentology, Stratigraphy and Palaeoenvironment of the Upper*
709 *Jurassic-Lower Cretaceous Non-Marine Strzelecki Group, Gippsland Basin,*
710 *Southeastern Australia*. Monash University. PhD Thesis.
- 711 Corti, G. (2004). Centrifuge modelling of the influence of crustal fabrics on the development
712 of transfer zones: Insights into the mechanics of continental rifting architecture.
713 *Tectonophysics*, 384, 191–208. <https://doi.org/10.1016/j.tecto.2004.03.014>
- 714 Corti, G. (2008). Control of rift obliquity on the evolution and segmentation of the main

- 715 Ethiopian rift. *Nature Geoscience*, 1(4), 258–262. <https://doi.org/10.1038/ngeo160>
- 716 Corti, G., van Wijk, J., Cloetingh, S., & Morley, C. K. (2007). Tectonic inheritance and
717 continental rift architecture: Numerical and analogue models of the East African Rift
718 system. *Tectonics*, 26(6), 1–13. <https://doi.org/10.1029/2006TC002086>
- 719 Corti, G., Philippon, M., Sani, F., Keir, D., & Kidane, T. (2013). Re-orientation of the
720 extension direction and pure extensional faulting at oblique rift margins: Comparison
721 between the Main Ethiopian Rift and laboratory experiments. *Terra Nova*, 25(5), 396–
722 404. <https://doi.org/10.1111/ter.12049>
- 723 Cruden, A. R., Nasser, M. H. B., & Pysklywec, R. (2006). Surface topography and internal
724 strain variation in wide hot orogens from three-dimensional analogue and two-
725 dimensional numerical models. *Geological Society Special Publications*, 253(1),
726 79–104. <https://doi.org/10.1144/GSL.SP.2006.253.01.04>
- 727 Daly, M. C., Chorowicz, J., & Fairhead, J. D. (1989). Rift basin evolution in Africa: the
728 influence of reactivated steep basement shear zones. *Geological Society, London,*
729 *Special Publications*, 44(1), 309–334. <https://doi.org/10.1144/GSL.SP.1989.044.01.17>
- 730 Davy, P., Hansen, A., Bonnet, E., & Zhang, S.-Z. (1995). Localization and fault growth in
731 layered brittle-ductile systems: Implications for deformations of the continental
732 lithosphere. *Journal of Geophysical Research: Solid Earth*, 100(B4), 6281–6294.
733 <https://doi.org/10.1029/94JB02983>
- 734 Davy, Ph, & Cobbold, P. R. (1991). Experiments on shortening of a 4-layer model of the
735 continental lithosphere. *Tectonophysics*, 188(1–2), 1–25. [https://doi.org/10.1016/0040-](https://doi.org/10.1016/0040-1951(91)90311-F)
736 [1951\(91\)90311-F](https://doi.org/10.1016/0040-1951(91)90311-F)
- 737 Deng, C., Gawthorpe, R. L., Finch, E., & Fossen, H. (2017). Influence of a pre-existing
738 basement weakness on normal fault growth during oblique extension: Insights from
739 discrete element modeling. *Journal of Structural Geology*.
740 <https://doi.org/10.1016/j.jsg.2017.11.005>
- 741 Deng, C., Gawthorpe, R. L., Fossen, H., & Finch, E. (2018). How Does the Orientation of a
742 Preexisting Basement Weakness Influence Fault Development During Renewed Rifting?
743 Insights From Three-Dimensional Discrete Element Modeling. *Tectonics*, 37(7), 2221–
744 2242. <https://doi.org/10.1029/2017TC004776>

- 745 Etheridge, M. A., Branson, J. C., & Stuart-Smith, P. G. (1985). Extensional basin-forming
746 structures in Bass Strait and their importance for hydrocarbon exploration. *The APEA*
747 *Journal*, 25, 344–361.
- 748 Faccenna, C., Nalpas, T., Brun, J. P., Davy, P., & Bosi, V. (1995). The influence of pre-
749 existing thrust faults on normal fault geometry in nature and in experiments. *Journal of*
750 *Structural Geology*, 17(8), 1139–1149. [https://doi.org/10.1016/0191-8141\(95\)00008-2](https://doi.org/10.1016/0191-8141(95)00008-2)
- 751 Finlayson, D. M., Johnstone, D. W., Owen, A. J., & Wake-Dyster, K. D. (1996). Deep
752 seismic images and the tectonic framework of early rifting in the Otway Basin,
753 Australian southern margin. *Tectonophysics*, 264(1–4), 137–152.
754 [https://doi.org/10.1016/S0040-1951\(96\)00123-0](https://doi.org/10.1016/S0040-1951(96)00123-0)
- 755 Fossen, H., & Tikoff, B. (1998). Extended models of transpression and transtension, and
756 application to tectonic settings. *Geological Society, London, Special Publications*,
757 135(1), 15–33. <https://doi.org/10.1144/GSL.SP.1998.135.01.02>
- 758 Ghosh, N., Hatui, K., & Chattopadhyay, A. (2020). Evolution of fault patterns within a zone
759 of pre-existing pervasive anisotropy during two successive phases of extensions: an
760 experimental study. *Geo-Marine Letters*, 40(1), 53–74. [https://doi.org/10.1007/s00367-](https://doi.org/10.1007/s00367-019-00627-6)
761 [019-00627-6](https://doi.org/10.1007/s00367-019-00627-6)
- 762 Gibson, G. M., Totterdell, J. M., White, L. T., Mitchell, C. H., Stacey, A. R., Morse, M. P., &
763 Whitaker, A. (2013). Pre-existing basement structure and its influence on continental
764 rifting and fracture zone development along Australia's southern rifted margin. *Journal*
765 *of the Geological Society*, 170(2), 365–377. <https://doi.org/10.1144/jgs2012-040>
- 766 Gray, D. R., Foster, D. A., Gray, C., Cull, J., & Gibson, G. (1998). Lithospheric Structure of
767 the Southeast Australian Lachlan Orogen along the Victorian Global Geoscience
768 Transect. *International Geology Review*, 40(12), 1088–1117.
769 <https://doi.org/10.1080/00206819809465256>
- 770 Heilman, E., Kolawole, F., Atekwana, E. A., & Mayle, M. (2019). Controls of Basement
771 Fabric on the Linkage of Rift Segments. *Tectonics*, 38(4), 1337–1366.
772 <https://doi.org/10.1029/2018TC005362>
- 773 Henza, A. A., Withjack, M. O., & Schlische, R. W. (2010). Normal-fault development during
774 two phases of non-coaxial extension: An experimental study. *Journal of Structural*

- 775 *Geology*, 32(11), 1656–1667. <https://doi.org/10.1016/j.jsg.2009.07.007>
- 776 Henza, A. A., Withjack, M. O., & Schlische, R. W. (2011). How do the properties of a pre-
777 existing normal-fault population influence fault development during a subsequent phase
778 of extension? *Journal of Structural Geology*, 33(9), 1312–1324.
779 <https://doi.org/10.1016/j.jsg.2011.06.010>
- 780 Heron, P. J., Peace, A. L., McCaffrey, K. J. W., Welford, J. K., Wilson, R., Hunen, J., &
781 Pysklywec, R. N. (2019). Segmentation of Rifts Through Structural Inheritance:
782 Creation of the Davis Strait. *Tectonics*, 38(7), 2411–2430.
783 <https://doi.org/10.1029/2019TC005578>
- 784 Hill, K. A., Cooper, G. T., Richardson, M. J., & Lavin, C. J. (1994). Structural framework of
785 the Eastern Otway basin: inversion and interaction between two major structural
786 provinces. *Exploration Geophysics*. <https://doi.org/10.1071/EG994079>
- 787 Hill, K. A., Finlayson, D. M., Hill, K. C., & Cooper, G. T. (1995). Mesozoic tectonics of the
788 Otway Basin region: the legacy of Gondwana and the active Pacific margin — a review
789 and ongoing research. *The APPEA Journal*, 35(1), 467–493.
790 <https://doi.org/https://doi.org/10.1071/AJ94030>
- 791 Holdsworth, R. E. (1989). Late brittle deformation in a caledonian ductile thrust wedge: new
792 evidence for gravitational collapse in the Moine Thrust sheet, Sutherland, Scotland.
793 *Tectonophysics*, 170(1–2), 17–28. [https://doi.org/10.1016/0040-1951\(89\)90100-5](https://doi.org/10.1016/0040-1951(89)90100-5)
- 794 Holdsworth, R. E., Butler, C. A., & Roberts, A. M. (1997). The recognition of reactivation
795 during continental deformation. *Journal of the Geological Society*, 154(1), 73–78.
796 <https://doi.org/10.1144/gsjgs.154.1.0073>
- 797 Kennett, B. L. N., Fichtner, A., Fishwick, S., & Yoshizawa, K. (2013). Australian
798 seismological referencemodel (AuSREM): Mantle component. *Geophysical Journal
799 International*, 192(2), 871–887. <https://doi.org/10.1093/gji/ggs065>
- 800 Kirkpatrick, J. D., Bezerra, F. H. R., Shipton, Z. K., Do Nascimento, A. F., Pytharouli, S. I.,
801 Lunn, R. J., & Soden, A. M. (2013). Scale-dependent influence of pre-existing basement
802 shear zones on rift faulting: a case study from NE Brazil. *Journal of the Geological
803 Society*, 170, 237–247. <https://doi.org/10.1144/jgs2012-043>
- 804 Kolawole, F., Atekwana, E. A., Laó-Dávila, D. A., Abdelsalam, M. G., Chindandali, P. R.,

- 805 Salima, J., & Kalindekafe, L. (2018). Active Deformation of Malawi Rift's North Basin
806 Hinge Zone Modulated by Reactivation of Preexisting Precambrian Shear Zone Fabric.
807 *Tectonics*, 37(3), 683–704. <https://doi.org/10.1002/2017TC004628>
- 808 Mandl, G., Jong, L. N. J., & Maltha, A. (1977). Shear zones in granular material. *Rock*
809 *Mechanics*, 9(2–3), 95–144. <https://doi.org/10.1007/BF01237876>
- 810 McClay, K. R., & White, M. J. (1995). Analogue modelling of orthogonal and oblique rifting.
811 *Marine and Petroleum Geology*, 12(2), 137–151. [https://doi.org/10.1016/0264-](https://doi.org/10.1016/0264-8172(95)92835-K)
812 [8172\(95\)92835-K](https://doi.org/10.1016/0264-8172(95)92835-K)
- 813 McLean, M. A., Morand, V. J., & Cayley, R. A. (2010). Gravity and magnetic modelling of
814 crustal structure in central Victoria: what lies under the Melbourne Zone? *Australian*
815 *Journal of Earth Sciences*, 57(2), 153–173. <https://doi.org/10.1080/08120090903416245>
- 816 Miller, J. M. L., Norvick, M. S., & Wilson, C. J. L. (2002). Basement controls on rifting and
817 the associated formation of ocean transform faults - Cretaceous continental extension of
818 the southern margin of Australia. *Tectonophysics*, 359(1–2), 131–155.
819 [https://doi.org/10.1016/S0040-1951\(02\)00508-5](https://doi.org/10.1016/S0040-1951(02)00508-5)
- 820 Molnar, N. E., Cruden, A. R., & Betts, P. G. (2017). Interactions between propagating
821 rotational rifts and linear rheological heterogeneities: Insights from three-dimensional
822 laboratory experiments. *Tectonics*, 36(3), 420–443.
823 <https://doi.org/10.1002/2016TC004447>
- 824 Molnar, N. E., Cruden, A. R., & Betts, P. G. (2018). Unzipping continents and the birth of
825 microcontinents. *Geology*, 46(5), 451–454. <https://doi.org/10.1130/G40021.1>
- 826 Molnar, N. E., Cruden, A. R., & Betts, P. G. (2019). Interactions between propagating rifts
827 and linear weaknesses in the lower crust. *Geosphere*, 15(5), 1617–1640.
828 <https://doi.org/10.1130/GES02119.1>
- 829 Moore, A. M. G., Stagg, H. M. J., & Norvick, M. S. (2000). Deep-water Otway Basin: A new
830 assessment of the tectonics and hydrocarbon prospectivity. *The APPEA Journal*, 66–85.
- 831 Moore, D. H., Betts, P. G., & Hall, M. (2016). Constraining the VanDieland microcontinent
832 at the edge of East Gondwana, Australia. *Tectonophysics*, 687, 158–179.
833 <https://doi.org/10.1016/j.tecto.2016.09.009>
- 834 Morley, C. K. (1999). How successful are analogue models in addressing the influence of

- 835 pre-existing fabrics on rift structure? *Journal of Structural Geology*, 21(8–9), 1267–
836 1274. [https://doi.org/10.1016/S0191-8141\(99\)00075-9](https://doi.org/10.1016/S0191-8141(99)00075-9)
- 837 Morley, C. K. (2010). Stress re-orientation along zones of weak fabrics in rifts: An
838 explanation for pure extension in “oblique” rift segments? *Earth and Planetary Science*
839 *Letters*, 297(3–4), 667–673. <https://doi.org/10.1016/j.epsl.2010.07.022>
- 840 Morley, C. K., Haranya, C., Phoosongsee, W., Pongwapee, S., Kornsawan, A., & Wonganan,
841 N. (2004). Activation of rift oblique and rift parallel pre-existing fabrics during
842 extension and their effect on deformation style: examples from the rifts of Thailand.
843 *Journal of Structural Geology*, 26(10), 1803–1829.
844 <https://doi.org/10.1016/j.jsg.2004.02.014>
- 845 Müller, R. D., Seton, M., Zahirovic, S., Williams, S. E., Matthews, K. J., Wright, N. M., et al.
846 (2016). Ocean Basin Evolution and Global-Scale Plate Reorganization Events Since
847 Pangea Breakup. *Annual Review of Earth and Planetary Sciences*, 44(1), 107–138.
848 <https://doi.org/10.1146/annurev-earth-060115-012211>
- 849 Norvick, M. S., & Smith, M. S. (2001). Mapping the plate tectonic reconstruction of southern
850 and southeastern Australia and implications for petroleum systems. *The APPEA Journal*,
851 41, 15–35.
- 852 Peace, A., Dempsey, E., Schiffer, C., Welford, J., McCaffrey, K., Imber, J., & Phethean, J.
853 (2018). Evidence for Basement Reactivation during the Opening of the Labrador Sea
854 from the Makkovik Province, Labrador, Canada: Insights from Field Data and
855 Numerical Models. *Geosciences*, 8(8), 308. <https://doi.org/10.3390/geosciences8080308>
- 856 Peace, A., McCaffrey, K., Imber, J., van Hunen, J., Hobbs, R., & Wilson, R. (2018). The role
857 of pre-existing structures during rifting, continental breakup and transform system
858 development, offshore West Greenland. *Basin Research*, 30(3), 373–394.
859 <https://doi.org/10.1111/bre.12257>
- 860 Philippon, M., Willingshofer, E., Sokoutis, D., Corti, G., Sani, F., Bonini, M., & Cloetingh,
861 S. (2015). Slip re-orientation in oblique rifts. *Geology*, 43(2), 147–150.
862 <https://doi.org/10.1130/G36208.1>
- 863 Philippon, Mélody, & Corti, G. (2016). Obliquity along plate boundaries. *Tectonophysics*,
864 693, 171–182. <https://doi.org/10.1016/j.tecto.2016.05.033>

- 865 Phillips, T. B., & McCaffrey, K. J. W. (2019). Terrane Boundary Reactivation, Barriers to
866 Lateral Fault Propagation and Reactivated Fabrics: Rifting Across the Median Batholith
867 Zone, Great South Basin, New Zealand. *Tectonics*, 38(11), 4027–4053.
868 <https://doi.org/10.1029/2019TC005772>
- 869 Phillips, T. B., Jackson, C. A. L., Bell, R. E., Duffy, O. B., & Fossen, H. (2016). Reactivation
870 of intrabasement structures during rifting: A case study from offshore southern Norway.
871 *Journal of Structural Geology*, 91, 54–73. <https://doi.org/10.1016/j.jsg.2016.08.008>
- 872 Power, M. R., Hill, K. C., Hoffman, N., Bernecker, T., & Norvick, M. (2001). The Structural
873 and Tectonic Evolution of the Gippsland Basin: Results from 2D Section Balancing and
874 3D Structural Modelling. In K. C. Hill & T. Bernecker (Eds.), *Eastern Australasian*
875 *Basins Symposium* (pp. 373–384). Melbourne: Petroleum Exploration Society of
876 Australia.
- 877 Power, M. R., Hill, K. C., & Hoffman, N. (2003). Structural inheritance, stress rotation,
878 overprinting and compressional reactivation in the Gippsland Basin - Tuna 3D seismic
879 dataset. *The APPEA Journal*, 43, 197–221.
880 <https://doi.org/https://doi.org/10.1071/AJ02010>
- 881 Pysklywec, R. N., & Cruden, A. R. (2004). Coupled crust-mantle dynamics and intraplate
882 tectonics: Two-dimensional numerical and three-dimensional analogue modeling.
883 *Geochemistry, Geophysics, Geosystems*, 5(10). <https://doi.org/10.1029/2004GC000748>
- 884 Ramberg, H. (1967). *Gravity, Deformation and the Earth's Crust, as Studied by Centrifuged*
885 *Models*. London: Academic Press.
- 886 Ranalli, G. (1995). *Rheology of the Earth* (2nd ed.). London: Chapman and Hall.
- 887 Ranalli, G. (2001). Experimental tectonics: From Sir James Hall to the present. *Journal of*
888 *Geodynamics*, 32(1–2), 65–76. [https://doi.org/10.1016/S0264-3707\(01\)00023-0](https://doi.org/10.1016/S0264-3707(01)00023-0)
- 889 Riller, U., Cruden, A. R., Boutelier, D., & Schrank, C. E. (2012). The causes of sinuous
890 crustal-scale deformation patterns in hot orogens: Evidence from scaled analogue
891 experiments and the southern Central Andes. *Journal of Structural Geology*, 37, 65–74.
892 <https://doi.org/10.1016/j.jsg.2012.02.002>
- 893 Roberts, A. M., & Holdsworth, R. E. (1999). Linking onshore and offshore structures:
894 Mesozoic extension in the Scottish Highlands. *Journal of the Geological Society*, 156,

- 895 1061–1064.
- 896 Rotevatn, A., Kristensen, T. B., Ksienzyk, A. K., Wemmer, K., Henstra, G. A., Midtkandal,
897 I., et al. (2018). Structural inheritance and rapid rift-length establishment in a multiphase
898 rift: the East Greenland rift system and its Caledonian orogenic ancestry. *Tectonics*,
899 *37*(6), 1858–1875. <https://doi.org/10.1029/2018TC005018>
- 900 Samsu, A., Cruden, A. R., Hall, M., Micklethwaite, S., & Denyszyn, S. W. (2019). The
901 influence of basement faults on local extension directions: Insights from potential field
902 geophysics and field observations. *Basin Research*, *31*(4), 782–807.
903 <https://doi.org/10.1111/bre.12344>
- 904 Samsu, A., Cruden, A. R., Micklethwaite, S., Grose, L., & Vollgger, S. A. (2020). Scale
905 matters: The influence of structural inheritance on fracture patterns. *Journal of*
906 *Structural Geology*, *130*(September 2019), 103896.
907 <https://doi.org/10.1016/j.jsg.2019.103896>
- 908 Schellart, W. P. (2000). Shear test results for cohesion and friction coefficients for different
909 granular materials: Scaling implications for their usage in analogue modelling.
910 *Tectonophysics*, *324*(1–2), 1–16. [https://doi.org/10.1016/S0040-1951\(00\)00111-6](https://doi.org/10.1016/S0040-1951(00)00111-6)
- 911 Schueller, S., & Davy, P. (2008). Gravity influenced brittle-ductile deformation and growth
912 faulting in the lithosphere during collision: Results from laboratory experiments.
913 *Journal of Geophysical Research: Solid Earth*, *113*(12), 1–21.
914 <https://doi.org/10.1029/2007JB005560>
- 915 Schueller, S., Gueydan, F., & Davy, P. (2005). Brittle-ductile coupling: Role of ductile
916 viscosity on brittle fracturing. *Geophysical Research Letters*, *32*(10), 1–4.
917 <https://doi.org/10.1029/2004GL022272>
- 918 Schueller, S., Gueydan, F., & Davy, P. (2010). Mechanics of the transition from localized to
919 distributed fracturing in layered brittle-ductile systems. *Tectonophysics*, *484*(1–4), 48–
920 59. <https://doi.org/10.1016/j.tecto.2009.09.008>
- 921 Sharples, W., Moresi, L.-N., Jadamec, M. A., & Revote, J. (2015). Styles of rifting and fault
922 spacing in numerical models of crustal extension. *Journal of Geophysical Research:*
923 *Solid Earth*, *120*, 4379–4404. <https://doi.org/10.1002/2014JB011813>.Received
- 924 Sibson, R. H. (1985). A note on fault reactivation. *Journal of Structural Geology*, *7*(6), 751–

- 925 754. [https://doi.org/10.1016/0191-8141\(85\)90150-6](https://doi.org/10.1016/0191-8141(85)90150-6)
- 926 Tommasi, A., & Vauchez, A. (2001). Continental rifting parallel to ancient collisional belts:
927 an effect of the mechanical anisotropy of the lithospheric mantle. *Earth and Planetary*
928 *Science Letters*, 185(1–2), 199–210. [https://doi.org/10.1016/S0012-821X\(00\)00350-2](https://doi.org/10.1016/S0012-821X(00)00350-2)
- 929 Vollgger, S. A., & Cruden, A. R. (2016). Mapping folds and fractures in basement and cover
930 rocks using UAV photogrammetry, Cape Liptrap and Cape Paterson, Victoria, Australia.
931 *Journal of Structural Geology*, 85, 168–187. <https://doi.org/10.1016/j.jsg.2016.02.012>
- 932 Weijermars, R., & Schmeling, H. (1986). Scaling of Newtonian and non-Newtonian fluid
933 dynamics without inertia for quantitative modelling of rock flow due to gravity
934 (including the concept of rheological similarity). *Physics of the Earth and Planetary*
935 *Interiors*, 43(4), 316–330. [https://doi.org/10.1016/0031-9201\(86\)90021-X](https://doi.org/10.1016/0031-9201(86)90021-X)
- 936 Wijns, C., Weinberg, R., Gessner, K., & Moresi, L. (2005). Mode of crustal extension
937 determined by rheological layering. *Earth and Planetary Science Letters*, 236, 120–134.
938 <https://doi.org/10.1016/j.epsl.2005.05.030>
- 939 Willcox, J. B., & Stagg, H. M. J. (1990). Australia's southern margin: a product of oblique
940 extension. *Tectonophysics*, 173, 269–281. [https://doi.org/10.1016/0040-1951\(90\)90223-](https://doi.org/10.1016/0040-1951(90)90223-U)
941 U
- 942 Willcox, J. B., Colwell, J. B., & Constantine, A. E. (1992). New ideas on Gippsland Basin
943 regional tectonics. In *Gippsland Basin Symposium 22-23 June 1992* (pp. 93–110).
944 Melbourne.
- 945 Williams, S. E., Whittaker, J. M., & Müller, R. D. (2011). Full-fit, palinspastic reconstruction
946 of the conjugate Australian-Antarctic margins. *Tectonics*, 30(6).
947 <https://doi.org/10.1029/2011TC002912>
- 948 Wilson, J. T. (1966). Did the Atlantic Close and then Re-open? *Nature*, 211, 676–681.
- 949 Wilson, R. W., Holdsworth, R. E., Wild, L. E., McCaffrey, K. J. W., England, R. W., Imber,
950 J., & Strachan, R. A. (2010). Basement-influenced rifting and basin development: a
951 reappraisal of post-Caledonian faulting patterns from the North Coast Transfer Zone,
952 Scotland. *Geological Society, London, Special Publications*, 335(1), 795–826.
953 <https://doi.org/10.1144/SP335.32>
- 954 Withjack, M., & Jamison, W. R. (1986). Deformation produced by oblique rifting.

- 955 *Tectonophysics*, 126, 99–124. <https://doi.org/https://doi.org/10.1016/0040->
956 1951(86)90222-2
- 957 Zwaan, F., & Schreurs, G. (2017). How oblique extension and structural inheritance influence
958 rift segment interaction: Insights from 4D analog models. *Interpretation*, 5(1), SD119–
959 SD138. <https://doi.org/10.1190/INT-2016-0063.1>
- 960 Zwaan, F., & Schreurs, G. (2020). Rift segment interaction in orthogonal and rotational
961 extension experiments: Implications for the large-scale development of rift systems.
962 *Journal of Structural Geology*, 140(March), 104119.
963 <https://doi.org/10.1016/j.jsg.2020.104119>
- 964 Zwaan, F., Schreurs, G., Naliboff, J., & Buitter, S. J. H. (2016). Insights into the effects of
965 oblique extension on continental rift interaction from 3D analogue and numerical
966 models. *Tectonophysics*, 693, 239–260. <https://doi.org/10.1016/j.tecto.2016.02.036>
- 967